HAL
open science

An experimental study of the brittle-ductile transition of basalt at oceanic crust pressure and temperature conditions

Marie Violay, Benoit Gibert, David Mainprice, Brian Evans, Jean-Marie Dautria, Pierre Azais, Philippe Pezard

To cite this version:

Marie Violay, Benoit Gibert, David Mainprice, Brian Evans, Jean-Marie Dautria, et al.. An experimental study of the brittle-ductile transition of basalt at oceanic crust pressure and temperature conditions. Journal of Geophysical Research, 2012, 117, pp.B03213. 10.1029/2011JB008884 . hal-00760905

HAL Id: hal-00760905

https://hal.science/hal-00760905v1

Submitted on 10 May 2021

HAL is a multi-disciplinary open access archive for the deposit and dissemination of scientific research documents, whether they are published or not. The documents may come from teaching and research institutions in France or abroad, or from public or private research centers.

L'archive ouverte pluridisciplinaire **HAL**, est destinée au dépôt et à la diffusion de documents scientifiques de niveau recherche, publiés ou non, émanant des établissements d'enseignement et de recherche français ou étrangers, des laboratoires publics ou privés.

An experimental study of the brittle-ductile transition of basalt at oceanic crust pressure and temperature conditions

Marie Violay,[1,2] Benoit Gibert,[1] David Mainprice,[1] Brian Evans,[3] Jean-Marie Dautria,[1] Pierre Azais,[1] and Philippe Pezard[1]

Received 21 September 2011; revised 10 January 2012; accepted 1 February 2012; published 23 March 2012.

[1] The brittle to ductile transition (BDT) in rocks may strongly influence their transport properties (i.e., permeability, porosity topology…) and the maximum depth and temperature where hydrothermal fluids may circulate. To examine this transition in the context of Icelandic crust, we conducted deformation experiments on a glassy basalt (GB) and a glass-free basalt (GFB) under oceanic crust conditions. Mechanical and micro-structural observations at a constant strain rate of 10^{-5} s^{-1} and at confining pressure of 100–300 MPa indicate that the rocks are brittle and dilatant up to 700–800°C. At higher temperatures and effective pressures the deformation mode becomes macroscopically ductile, i.e., deformation is distributed throughout the sample and no localized shear rupture plane develops. The presence of glass is a key component reducing the sample strength and lowering the pressure of the BDT. In the brittle field, strength is consistent with a Mohr-Coulomb failure criterion with an internal coefficient of friction of 0.42 for both samples. In the ductile field, strength is strain rate- and temperature-dependent and both samples were characterized by the same stress exponent in the range $3 < n < 4.2$ but by very different activation energy $Q_{GB} = 59 \pm 15$ KJ/mol and $Q_{GFB} = 456 \pm 4$ KJ/mol. Extrapolation of these results to the Iceland oceanic crust conditions predicts a BDT at ~100°C for a glassy basalt, whereas the BDT might occur in non-glassy basalts at deeper conditions, i.e., temperatures higher than 550 ± 100°C, in agreement with the Icelandic seismogenic zone.

Citation: Violay, M., B. Gibert, D. Mainprice, B. Evans, J.-M. Dautria, P. Azais, and P. Pezard (2012), An experimental study of the brittle-ductile transition of basalt at oceanic crust pressure and temperature conditions, *J. Geophys. Res.*, *117*, B03213, doi:10.1029/2011JB008884.

1. Introduction

[2] The mid-ocean ridge system is the largest continuous volcanic feature on Earth, with significant interactions between tectonic activity, volcanism and seawater circulation [*Macdonald*, 1982]. At mid-ocean ridges, new crust is formed and cools by heat conduction and by hydrothermal circulation [e.g., *Johnson et al.*, 1993; *Phipps Morgan and Chen*, 1993; *Stein and Stein*, 1994]. Seawater penetrates into the upper crust, and is heated as it moves down toward the base of the sheeted dike complex, in the vicinity of the magma chamber [e.g., *Teagle et al.*, 1998]. The discharge of hydrothermal fluids occurs along the ridge axis at temperatures up to ~400°C [e.g., *Koschinsky et al.*, 2008]. At seafloor the fluid is replaced by seawater "recharge," creating a circulation cell. During the circulation, the seawater reacts with oceanic crustal rocks, leading to important processes such mineral dissolution/precipitation and heat exchanges [e.g., *Edmond et al.*, 1982; *Alt et al.*, 1996]. There are some economic uses of hydrothermal circulation, as for example geothermal power [e.g., *Pálmason and Sæmundsson*, 1979] and mining ore deposits [*Nelson and Giles*, 1985; *Mills and Elderfield*, 1995]. To better understand the dynamics of seawater circulation, a fundamental question to be considered is maximum pressure and temperature at which hydrothermal fluids may penetrate by a cracking front at mid-oceanic ridges in the axial region above the axial magma chamber and off axis [*Lister*, 1980; *Stein and Stein*, 1994; *Elderfield and Schultz*, 1996; *Manning et al.*, 1996; *Nicolas et al.*, 2003]. Seawater circulation within the upper oceanic crust depends on the transport properties of oceanic crustal rocks (permeability, porosity topology…), which is strongly influenced by the deformation mode of the crust, i.e., brittle versus ductile deformation, which vary according to a wide range of pressure and temperature conditions [*Lockner and Madden*, 1991; *Fischer and Paterson*, 1992; *Morrow and Lockner*, 1994, 1997; *Morrow et al.*, 1994; *Zhu et al.*, 2007; *De Paola et al.*, 2009]. Indeed, cracks and fractures control the bulk permeability of oceanic crust,

[1]Géosciences Montpellier UMR 5243, CNRS, Université Montpellier 2, Montpellier, France.
[2]Now at Istituto Nazionale di Geofisica e Vulcanologia, Rome, Italy.
[3]Department of Earth, Atmospheric, and Planetary Sciences, Massachusetts Institute of Technology, Cambridge, Massachusetts, USA.

Copyright 2012 by the American Geophysical Union.
0148-0227/12/2011JB008884

providing critical pathways for hydrothermal fluids and magma [e.g., *Norton and Knapp*, 1977; *Lowell et al.*, 1995; *Singh et al.*, 1999; *Tolstoy et al.*, 2008].

[3] A partial answer to this question can consequently be provided by the determination of the pressure and temperature of the brittle to ductile transition in oceanic crust rocks, as this depth is often considered to correspond to a significant modification of the porosity topology [*Hirth et al.*, 1998; *Hirose and Hayman*, 2008; *Nara et al.*, 2011].

[4] Our current understanding of mid ocean ridge, has been aided by geophysical observation and rheological modeling. On one hand, heat flux measurements and seismic studies show that (i) hydrothermal circulation up to 700°C must be taken into account to explain the cooling of the oceanic crust [*Sleep and Rosendahl*, 1979; *Chen and Morgan*, 1990; *Phipps Morgan and Chen*, 1993; *Stein and Stein*, 1994; *Fontaine et al.*, 2001, 2008] (ii) the lower limit of the oceanic crust seismogenic zone occurs at about 700°C [*Ranero et al.*, 1997; *Ágústsson and Flovenz*, 2005; *Bjornsson*, 2008]. On the other hand, the rheological model of oceanic crust is poorly constrained due the limited number of experimental mechanical studies of oceanic crustal rocks (basalts, dolerites, gabbros). This paucity is in part due to the difficulty in locating samples with appropriate microstructures for the laboratory experiments. Most gabbros of the lower oceanic crust have grain sizes (>1 cm) that are too large for studies in conventional deformation machines, and most basalts contain too much glassy component (>25%) to provide realistic flow laws. In order to constrain the rheological properties of basaltic crust, most experimental work has focused on monocrystals or single-phase aggregates of typical minerals such as plagioclases [*Borg and Heard*, 1969, 1970; *Marshall and MacLaren*, 1977a, 1977b; *Tullis and Yund*, 1977, 1980, 1987, 1991; *Dell'Angelo et al.*, 1987; *Dell'Angelo and Tullis*, 1988; *Dimanov et al.*, 1998, 1999, 2000; *Rybacki and Dresen*, 2004], pyroxene [*Avé Lallement*, 1978; *Kollé and Blacic*, 1982, 1983; *Kirby and Kronenberg*, 1984; *Dimanov et al.*, 2003; *Dimanov and Dresen*, 2005; *Moghadam et al.*, 2010], and olivine [*Goetze and Brace*, 1972; *Kohlstedt and Goetze*, 1974; *Weertman and Weertman*, 1975; *Hirth and Kohlstedt*, 1995; *Zimmerman and Kohlstedt*, 2004]. There are also relatively few studies on deformation mechanisms of polyphasic diabases and gabbros [*Kronenberg and Shelton*, 1980; *Shelton and Tullis*, 1981; *Caristan*, 1982; *Shimada et al.*, 1989; *Hacker and Christie*, 1992; *Mackwell et al.*, 1998; *He et al.*, 2007] and polyphasic synthetic gabbros [*Dimanov and Dresen*, 2005; *Dimanov et al.*, 2007, 2011]. These studies were performed at very high temperatures and pressures, far from the in situ oceanic crust conditions. *Hacker and Christie* [1992] provide data at very high pressure (>1 GPa) on basalts under brittle and ductile conditions, but at temperatures where the glassy component dominate the deformation process. Deformation experiments on Maryland diabase by *Mackwell et al.* [1998] and *Caristan* [1982] provide some rheological information, but only at high temperature (>900°C).

[5] In this paper, we present new data on rheological properties of basalt at oceanic in situ crustal P,T conditions i.e., at confining pressure from 100 to 300 MPa, temperature from 400°C to 950°C, and pore fluid pressure from 0 to 50 MPa. Two samples were selected for their low porosity (<3%), their variation in glassy component (glassy basalt/glass free basalt) and their low degree of alteration. Both samples are representative of a thick basaltic crust formed by a successive stacking of partly glassy volcanic lava flows as Iceland, or Hawaii crust [*Kaban et al.*, 2002; *Moore et al.*, 1982]. Glassy basalt are also common in oceanic crust as showed at ODP hole 896A located south of the Costa Rica Rift [*Fisk et al.*, 1996].

2. Methods

2.1. Experimental Methods

[6] Cylindrical samples of 10 mm in diameter and 20 mm in length were jacketed with copper or iron after being dried over 48 h at 70°C. These assemblies were then deformed in conventional triaxial experiments conducted in a servo-controlled, gas-medium apparatus from "Paterson instruments." Temperatures ranged from 400°C to 950°C; confining pressures (P_c) from 100 MPa to 300 MPa, and pore pressures (P_p) from 0 to 50 MPa. Both water and argon were used as pore fluids. Deformation experiments were generally performed up to strains of 15% with constant strain rate ($\dot{\varepsilon}$), where $10^{-6}\ s^{-1} \leq \dot{\varepsilon} \leq 10^{-4}\ s^{-1}$. The constant strain rate portion of the tests was usually followed by stress relaxation to evaluate the strain rate sensitivity of stress, but in some experiments, the imposed deformation rate was changed to a new value. Differential stresses were measured with an accuracy of 2 MPa. To reduce jacket strength, copper was used at low temperatures (400 to 750°C), whereas iron jackets were used above that range. Corrections were applied to the measured force using jacket strengths estimated from *Frost and Ashby* [1982] and from the change in sample dimensions with deformation; displacement measurements were corrected for apparatus distortion.

2.2. Analytical Methods

[7] After deformation, samples were impregnated with epoxy and then cut parallel to the cylinder axis, or, if deformation was localized, perpendicular to the shear zone. From each sample, a polished, 30 μm, thin section was prepared and examined in an optical microscope using plane-polarized, cross-polarized and reflected light, and in a scanning electron microscope (SEM). Chemical and crystallographic information were collected by EPMA microanalysis and electron backscattered diffraction (EBSD) in SEM.

[8] Textural observations and chemical analyses of crystals and glass were done at "Service Microsonde Sud" (Université Montpellier 2) using a five-spectrometer CAMECA SX100 electron microprobe. The analyses were undertaken at 20 kV accelerating voltage, a beam current of 10 nA, and counting times of 20–30 s. Concentrations are obtained from raw intensities using the "X-PHI" quantification procedure [*Merlet*, 1994] and standards of natural minerals, synthetic oxides, and pure metals. The spots to be analyzed were selected in the backscattered electron (BSE) mode to ensure that only single phases were analyzed and to facilitate the identification of phases and compositional zoning.

[9] Element detection limits are a function of phase composition, volatile contents, the surface polish of thin sections, and grain size. Phase identification and characterization of

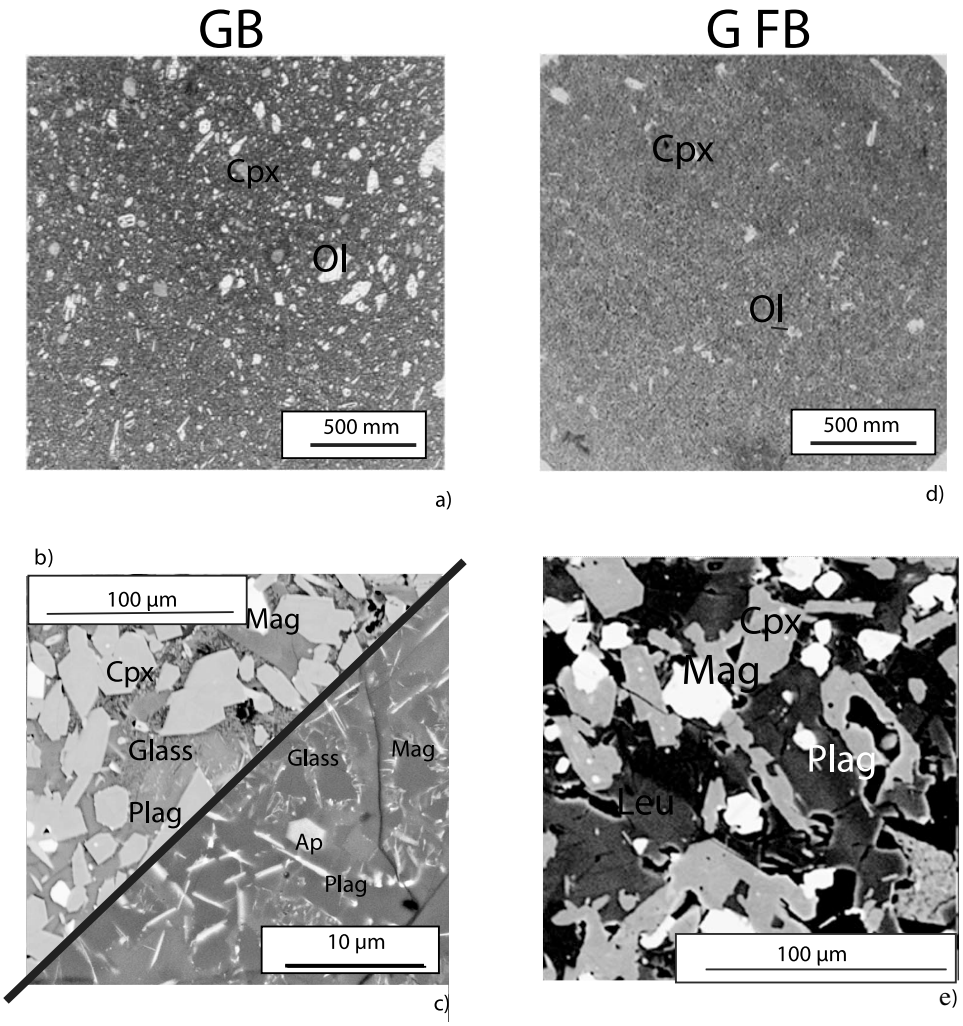

Figure 1. Thin-section photographs of (a–c) GB and (d, e) GFB starting sample at different scale. Figures 1a, 1b, 1d, and 1e show thin sections on optical plane-polarized light micrograph. Figure 1c shows Backscattered Scanning Electron microphotograph. Ol: olivine, Cpx: clinopyroxene, Plag: plagioclase, Mag: magnetite, Ap: apatite, Leu: leucite.

microstructures were done using an FEI Quanta 200 SEM operating in BSE mode; additional observations were done in a CamScan X500FE CrystalProbe, Electron Backscattered Diffraction microscope to identify phases, to examine the crystallographic orientation, and to elucidate rock texture. Crystal indexing was performed both manually and automatically. Detection of orientation is possible in grains larger than 0.1 micron, depending on surface polish, thickness of the thin sections, and presence of glass.

3. Starting Material

3.1. Glassy Basalt

[10] The first suite of glassy basalt (GB) samples came from the caprock of the Deves lava flow, Sénouire valley, France, a microlithic, porphyritic basalt containing about 20 vol % phenocrysts of clinopyroxene and olivine. The remaining groundmass contains phonolitic glass (15–25 vol %) and fine-grained crystalline phases including plagioclase (24–32 vol % of the total rock), clinopyroxene (32–40 vol %), and other oxides (4–8 vol %) (Figure 1 and Table 1). This modal composition is uniformly distributed at the thin-section scale. The glass component could be identified by the presence of potassium, which is segregated into that phase. By contrast, the crystalline silicate and oxide phases contain less than 0.1 wt % potassium. Thus, the glass quantity was estimated by calculating the mass balance of potassium oxide between bulk rock and glass:

$$[K_2O]_{\text{bulk rock}}/[K_2O]_{\text{glass}} = [\text{Glass}]_{\text{bulk rock}} \quad (1)$$

Glass abundance was also determined by point counting on optical thin-sections (minimum 300 points per thin section). Both methods suggest that these rocks contain 20 ± 5 vol % glass.

[11] The olivine phenocrysts are subhedral, equant glomerocrysts of Fo79; these are typically 1–2 mm in diameter, corroded at their peripheries and partially altered to iddingsite. The clinopyroxene phenocrysts are subhedral laths or prisms of augite that are, on average, 1 mm in length. Compositional zoning of titanium within the orthopyroxene crystals is very common. In the clinopyroxene phase,

Table 1. Mineralogical and Petrophysical Characteristics of GB and GFB Samples

Sample	Phenocrysts Mineralogy	Phenocrysts Grain Size	Groundmass Mineralogy	Groundmass Grain Size	Percentage of Glass	Percentage of Alteration	Secondary Minerals	Porosity (%)	Density
GB	clinopyroxene; olivine	1–3 mm; 1–2 mm	plagioclase; clinopyroxene; oxides	≈50–200 μm; ≈10–100 μm; ≈2–10 μm	≈15–25%	1–3%	iddingsite	2.4%	3.0
GFB	clinopyroxene; olivine	500 μm–1,5 mm; 200–500 μm	plagioclase; felspathoid; clinopyroxene; oxides	≈20–80 μm; ≈30–70 μm; ≈10–100 μm; ≈2–10 μm	≈0%	1–3%	iddingsite	2.3%	2.9

groundmass crystals are slightly more titaniferous than phenocrysts. The grain size of the clinopyroxene phase present in groundmass is ~10–100 μm. Plagioclases are subhedral to euhedral labradorite laths up to 100 μm long. Oxides are mainly titanomagnetite, with a few ilmenites. The EPMA analyses indicate that the glass fraction contains about 2–3% of volatiles. Thermo-gravimetric measurements up to 1200°C show that the GB samples contain 0.6 wt % volatiles. Thermo-gravimetric measurements did not detect the temperature of the glass transition in GB glass. The glass also contains microliths, less than 10 μm long, of titanomagnetite, ilmenite and apatite. The starting material does not contain hydrous minerals. Porosity was measured by using the classical triple-weighing method. Samples were first weighed after being dried in an oven at ~50°C (>72 h) and re-saturated for "wet" weight measurements in vacuum and immersed in water, flooding the accessible connected porosity. Porosity is 2.4% ± 0.2%. (Figure 1 and Table 1).

3.2. Glass-Free Basalt

[12] A second set of samples, which are glass-free (GFB), were taken from columnar basalts in the Escandorgue flow, Languedoc-Roussillon, France. These rocks are micro- to crypto-crystalline basalts containing approximately 5 vol. % of phenocrysts (essentially clinopyroxenes and a few olivines). Thermo-gravimetric measurements up to 1200°C show that the GFB samples do not contain volatiles. The remaining fine-grained groundmass (Figure 1 and Table 1) is a homogeneous mixture of plagioclase (35–45 vol. % of the total rock), clinopyroxene (25–35%) feldspathoids (10%), and titanomagnetite (5–15%). Olivine phenocrysts are subhedral, equant glomerocrysts of Fosterite (Fo79), about 300 μm in diameter. Clinopyroxene (Cpx) phenocrysts are subhedral laths or prisms of augite, about 100 μm long; compositional zoning of titanium is very common. Clinopyroxene crystals in the groundmass (grain size ~10–100 μm) are slightly more titaniferous than clinopyroxene phenocrysts (grain size ~200–500 μm). In the groundmass, plagioclases are subhedral laths with composition varying from labradorite to oligoclase. The feldspathoids are euhedral laths of leucite and nepheline, averaging 50 μm in length. Over scales less than 1 mm, there is local preferred orientation of the feldspathoid and plagioclase crystals, probably due to magmatic flow (Figure 1 and Table 1). Porosity measured by triple weighing is (2.3%).

4. Mechanical Data

[13] We conducted 34 triaxial deformation experiments under various conditions of T, P_c, P_p, and strain rate (Table 3). The reproducibility of strength measured in sets of experiments performed at nominally identical conditions indicates sample-to-sample variability (due to porosity, and petrological variability) of about ±50 MPa for both GB and GFB sample suites, a value well above the precision of 2 MPa (Figures 2e and 2f). Strength values quoted in the following sections are for constant strain rate of 10^{-5} s^{-1}, unless stated otherwise.

[14] To simplify the results section we will only present the experiments where P_p = 0 MPa. Others results ($P_p \neq 0$) are given Table 3 and Figures 6 and 7.

4.1. Glassy Basalt

[15] In the vitreous samples, elastic behavior at very low strains is followed by one of four deformation modes, depending on temperature, pressure and strain rate (Figures 2a and 2b):

[16] 1. At 400°C and confining pressure (P_c) of 100 MPa, the sample (GB1) yields at about 350 MPa, and then rapidly hardens to peak stress of 900 MPa at strain of 5%, followed by strain weakening (Figure 2a).

[17] 2. Between 500°C to 700°C (GB2, GB3, GB9), at a confining pressure of 100 MPa, samples yield at stresses that depend on temperature, followed by modest, monotonic hardening up to stresses of 200 ± 20 MPa, at strains of 10%. The strength of the samples at the end of the experiment also depends on temperature, although there is one discrepant result at 700°C (Figure 2a).

[18] 3. In one experiment at 800°C and P_c = 100 MPa (GB12), the strength was inversely proportional to strain rate, and this sample exhibited localization and may also have been strain weakening (Figure 3a). Other samples deformed at 800°C (GB10, GB11) harden monotonically with strain and exhibited distributed deformation. Strain rate stepping experiments at 800°C and P_c = 100 MPa indicate that strength is directly correlated with strain rate even when a constant hardening coefficient is assumed (Figure 3b).

[19] 4. At 900°C, at P_c = 100 MPa (GB14), or between 600–900°C at P_c = 300 MPa (GB16, GB17, GB19, GB20), peak strengths at the end of the experiment are from 30 to 100 MPa. The samples harden monotonically with strain at all temperatures, but the hardening coefficient systematically decreases from 600 to 750°C and becomes small at higher temperatures (Figure 2b).

4.2. Glass-Free Basalt

[20] For the glass-free samples, yielding occurs at strains larger than the GB samples, but which are still <2%; yield is followed by one of two deformation modes, depending on temperature and pressure (Figures 2c and 2d):

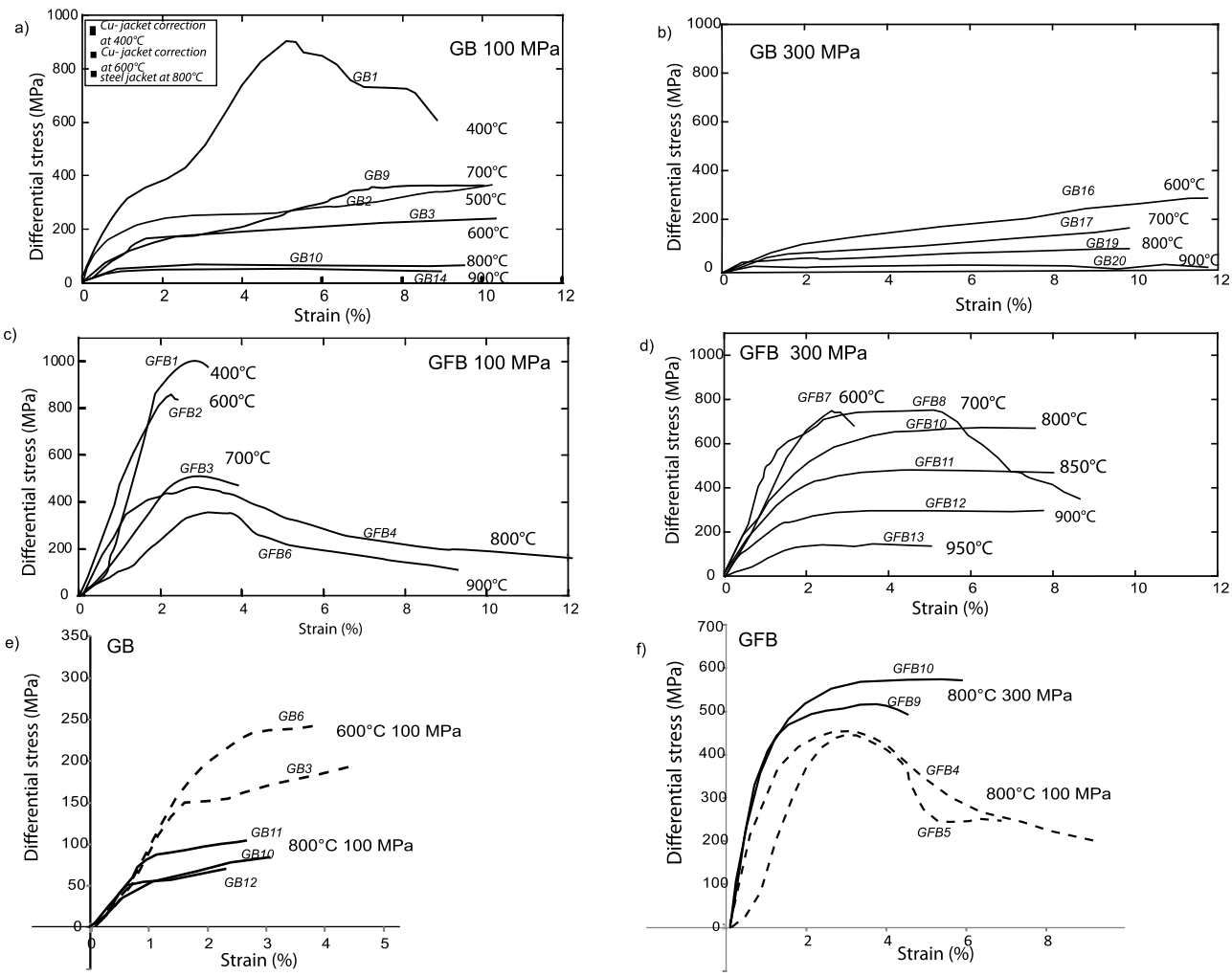

Figure 2. Differential stress versus strain curves for experiments conducted at temperature between 400 and 900°C and confining pressure from 100 to 300 MPa. The initial strain rate for all experiments was 10^{-5} s^{-1}. (a) GB sample at 100 MPa, (b) GB sample at 300 MPa, (c) GFB sample at 100 MPa, (d) GFB sample at 300 MPa (e) GB reproducibility, and (f) GFB reproducibility.

[21] 1. Between 600–900°C (GFB1, GFB2, GFB3, GFB4, GFB6) at P_c = 100 MPa, or between 600–800°C at 300 MPa (GFB7, GFB8, GFB9), the peak strength depends directly on temperature, but the effect of pressure is not so easily characterized. Peak stress is systematically followed by strain weakening up to strains of about 5–10% (Figures 2c and 2d). Strain rate stepping tests suggest that strength has low strain rate sensitivity, but the strength is also evolving with strain during the experiment, complicating the interpretation (Figure 3c).

[22] 2. At the highest temperatures, 800°C to 950°C (GFB10, GFB11, GFB12 and GFB13), and P_c = 300 MPa, the peak strength clearly decreases with T (Figure 2d), and hardening coefficients are low. Strain rate stepping experiments suggest that strength has low strain rate sensitivity (Figure 3d).

5. Deformation Textures and Microstructures

[23] After experiments, thin sections were cut so that they contained the shear direction and the sample axis; these were studied using optical, Scanning Electron (SEM) and Electron backscattered diffraction (EBSD) microscopy (see methods and Figures 1, 4, and 5).

5.1. Glassy Basalt

[24] At lower confining pressures, e.g., 100 MPa and 400 < T < 800°C (Figure 4, first column), strain was localized, often along a main fault associated with smaller subparallel or intersecting cracks and faults. At the lowest pressure and temperature (100 MPa, 400°C), glassy basalt samples failed by axial wedge splitting. At 500 < T < 700°C, anastomising shear bands about 100 to 500 μm thick developed. Their thickness increased as P_c decreased or T increased. Most of the shear bands were oriented between 30° and 40° to the compression direction, the angle increasing as temperature increased. Within the shear zone, a cataclastic foliation developed by grain-size reduction, micro-cracking, and rigid-rotation and frictional sliding of fragments (Figure 4, second and third columns). The fault zones contained angular fragments ranging from 0.01 to 10 μm; the faults became irregular in shape and orientation when they intersected phenocrysts. Some phenocrysts in or

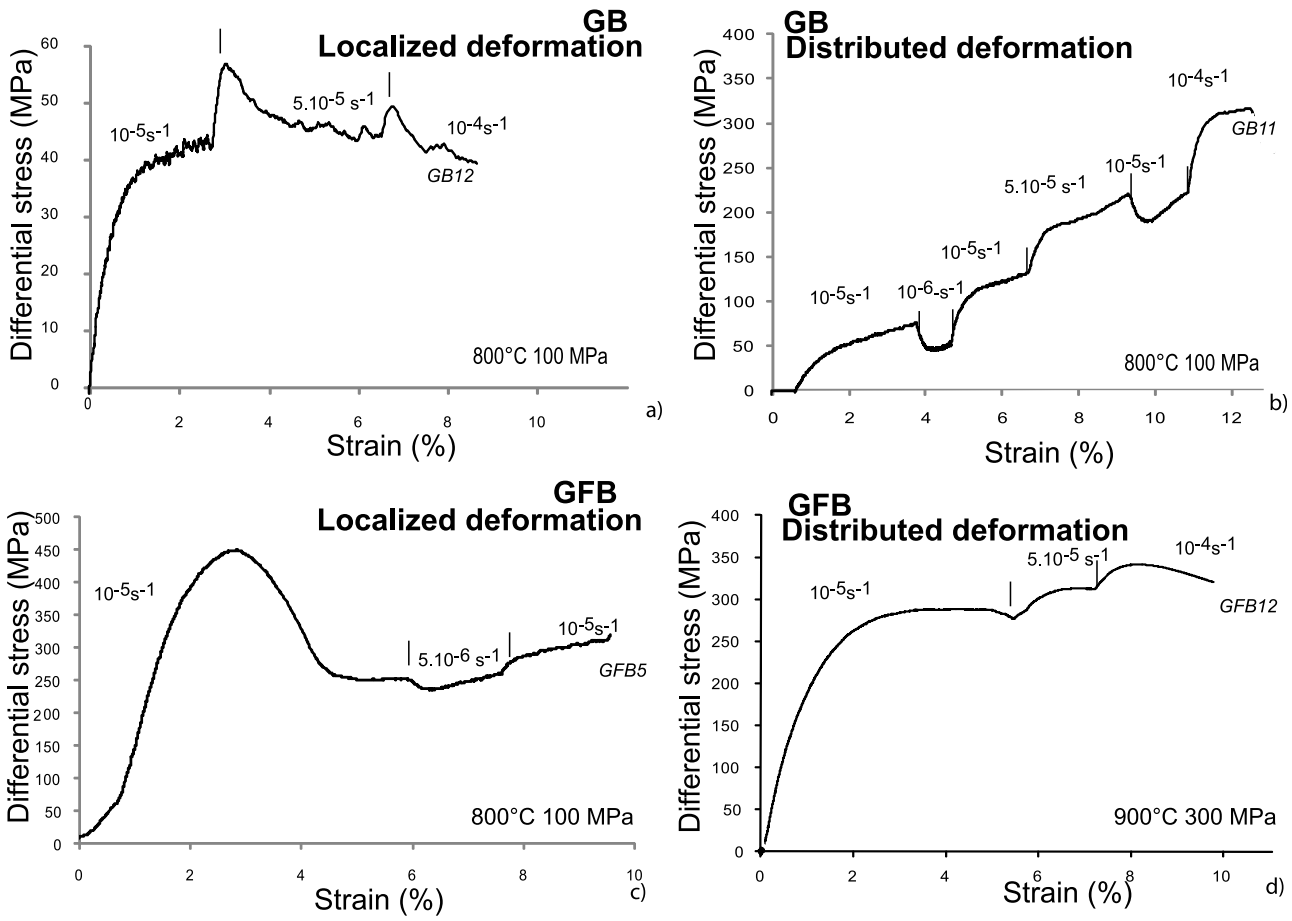

Figure 3. Differential stress versus strain curves for experiments conducted at different strain rates in order to evaluate the strain rate sensitivity on stress. (a, b) GB sample (c, d) GFB sample.

near the shear zone were broken *en échelon*. Another notable phenomenon was the disappearance of opaque impurities in olivine grains (iddingsite), and the appearance of gray halos on the boundary of some titanomagnetite (Figure 4).

[25] At the highest temperatures and pressures (P_c = 100 MPa and 800 < T < 900°C; or P_c = 300 MPa and 600 < T < 900°C), macroscopically distributed deformation was observed. But, even at the highest temperatures, the characteristic features of intracrystalline deformation rarely observed. At 600 < T < 800°C and P_c = 300 MPa, the glassy basalt deformed by a combination of diffuse micro-cracking of minerals and the glassy groundmass (at 600°C) (image 6 in Figure 4). Cracks were often oriented between 30° and 40° to compression direction, and this angle increased as the temperature increased. Accepting the alteration of the iddingsite and titanomagneitite phases mentioned above, metamorphic changes in the other major phases were difficult to recognize because of the wide compositional variations in the starting materials. For example, pyroxene and feldspar crystals are often zoned. However, samples deformed at 100 and 300 MPa and 800 < T < 900°C, show evidence that the glass partially recrystallized to biotite and nepheline, a change accompanied by the disappearance of oxides initially contained in the glass and the destabilization of augite. The dark mica now occurs as subhedral laths or spheres ≤ 0.5 μm, and the nepheline crystals are anhedral and less than 0.3 μm in diameter (Figure 4, fourth column). Due to their very small size, the micas and nepheline crystals were difficult to analyze by EPMA. The glass volume fraction did not change during deformation, but the chemical composition of the residual glass did change as function of temperature (cf. Tables 2–3). At 900°C, the Fe_2O_3 and CaO contents increased by 6.2% and 2.8%, respectively, while NaO and Al_2O_3 contents decreased by 4.2% and 5.4%, respectively. These changes are coherent with the mineralogical observations: partial dissolution of augite released calcium, aluminum and sodium oxides, which then crystallized as nepheline.

[26] Using an SEM at Geosciences Montpellier, we performed Electron Backscattered Diffraction (EBSD) observations to measure the effect of deformation on the crystal-preferred orientations (CPO) of clinopyroxene and plagioclase. Three maps of about 1 mm^2 were made for each of three thin sections: the starting material and samples deformed at 300 MPa and 600°C or 800°C. The automatic mapping used a regular grid step of 1 μm, which is about 100 times smaller than the largest observed matrix grains. Map locations were chosen to sample the GB groundmass and to avoid phenocrysts. The automated process successfully indexed about 35–45% of the pixels. That fraction could be increased to 50–60% by manual indexing, but the CPO patterns obtained automatically and manually were the

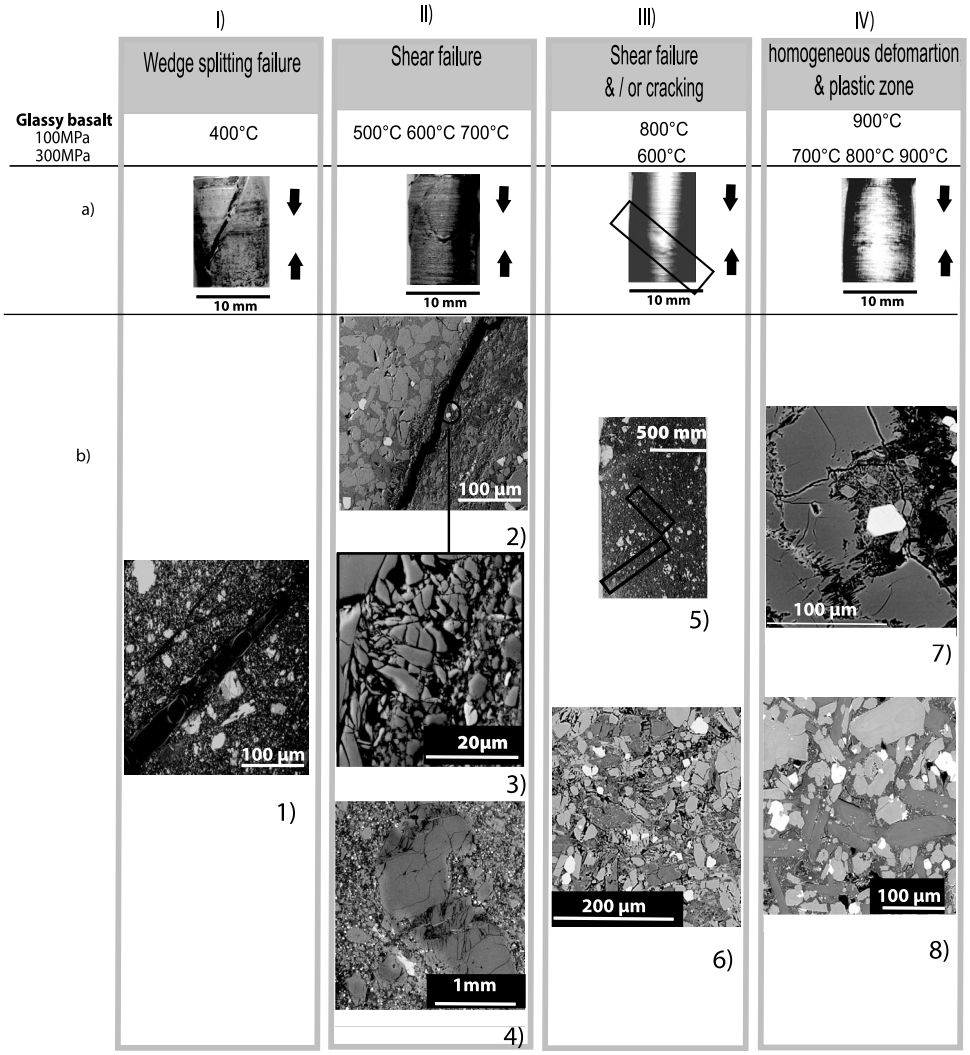

Figure 4. (a) Photographs of post-run jacketed GB sample (b) thin section photograph of GB samples deformed under different physical conditions. Images 1 and 5 show optical plane-polarized light micrograph; images 2–4 and 6–8 show Backscattered Scanning Electron microphotograph.

same. Non-indexed pixels were usually located on regions of poor polishing, grain boundaries, glass, or unexpected minor phases like apatite.

[27] The clinopyroxene CPO in the starting material had density maxima for [100], [010] and [001] that were, respectively, 1.8, 1.3, and 1.7 times that of a uniform distribution. Plagioclase CPO maxima in the undeformed samples were 3.2, 4.8, 2.8 times random. Pole densities for both plagioclase and clinopyroxene decreased as the deformation temperature increased from 600 to 900°C. At 900°C, plagioclase maxima decreased to 1.8, 2.3, 1.7, for [100], [010], and [001]. The clinopyroxene maxima decreased more modestly: 1.5, 1.3 and 1.7. The subsequent clinopyroxene grains appeared to have rotated, and, indeed, the CPO suggests a rotation of 45° for [100] and [010], but the azimuth of [001] did not change.

5.2. Glass-Free Basalt

[28] The transitions in failure mode in the glass-free basalt were generally similar to those in the glassy basalt, except that localized deformation in GFB was favored to higher pressure and temperature. When P_c = 100 MPa, deformation was localized at all temperatures; when P_c = 300 MPa, localization also occurred at 600 < T < 800°C (Figure 5, columns 1–4). Deformation was distributed only when 800 < T < 950°C and P_c = 300 MPa.

[29] At 400 to 700°C, axial wedge-splitting occurred for all P_c. At 800 to 900°C at 100 MPa and 600 to 700°C at 300 MPa, GFB samples failed by forming localized, *en échelon*, shear fractures. These shear zones were oriented between 30° to 45° to the compression direction and contained brittle cataclastic micro-structures (Figure 7c). The angular fragments in the shear zones are now between 0.01 μm to 10 μm in diameter, reduced from the initial grain size of 100–500 μm. Shear zones are wider in the center of the sample than near its outer surface. Within the zones, plagioclase and oxide grains are aligned, forming black and white mottling. Oxides are strongly elongated and a series of cracks formed along the edge of the thin section (Figure 5, second column).

[30] At the highest pressure, 300 MPa, and temperatures, 800°C to 950°C, deformation was distributed. Indications of

Table 2. Chemical Composition of the Glass of GB Starting Material and GB Deformed Samples

	Sample									
	SiO_2	Al_2O_3	TiO_2	Na_2O	MgO	MnO	FeO	K_2O	CaO	Total
Starting material	51.28	23.69	1.31	9.47	0.80	0.10	4.82	5.57	1.07	98.30
Deformed sample at 600°C	50.06	23.07	1.62	8.74	1.22	0.13	6.61	4.95	1.55	98.20
Deformed sample at 700°C	49.75	20.43	2.23	5.84	2.34	0.14	6.46	4.30	6.26	98.25
Deformed sample at 800°C	50.32	18.86	1.38	2.38	2.12	0.10	9.72	8.02	2.68	97.20
Deformed sample at 900°C	52.48	18.23	2.66	5.26	1.73	0.15	11.21	4.99	3.85	100.67

intracrystalline deformation are rare, and no compositional or mineralogical changes were recognized. Oxides did not show textural or chemical changes (Figure 5, fourth column). Each sample contained a network of interpenetrating micro-faults oriented between 30 and 40°. Also, the porosity decreased by about 1–2%.

6. The Brittle and Ductile Domains

6.1. General Remarks About Mechanism and Mode of Semi-brittle Deformation

[31] To provide generalized formulations of rock strength, researchers often use a few simple constitutive laws meant to describe deformation by a single mechanism [*Kohlstedt et al.*, 1995]. These largely empirical laws are often derived from low-temperature tests of compact rocks, i.e., rocks with low porosity and without partial melts. For example, the shear stress, τ, necessary to cause sliding along a pre-existing fault at relatively low temperatures is given by Amonton's rule:

$$\tau = C + \mu\sigma_n \tag{2}$$

where μ is the coefficient of friction, C is a constant, and σ_n is the normal stress on the fault [*Paterson and Wong*, 2005]. *Byerlee* [1978] discovered that μ is relatively insensitive to rock type, at least at low temperatures without added fluids. Thus, he proposed that a simple combination of two linear equations of the form (1) could be used to constrain frictional sliding in natural situations.

[32] Brittle failure by localized rupture in compact rocks at low temperatures can be described using the Coulomb failure criterion [*Lockner*, 1995]. Thus, under conventional triaxial loading, the peak differential stress, σ_1–σ_3, is related to confining pressure, P_c, by

$$(\sigma_1 - \sigma_3) = \sigma_o + \mu' P_c \tag{3}$$

where $\sigma_2 = \sigma_3 = P_c$. The constants, μ' and σ_o, can be transformed to relate shear stress and normal stress on the rupture plane, yielding an equation of the form equation (3). The transformed constants are the internal coefficient of friction, μ_c, and the cohesive strength, C_{coh}, and are related to μ' and σ_o [*Paterson and Wong*, 2005]:

$$\mu_c = \mu' / \left(2\sqrt{(1+\mu')}\right) \tag{4}$$

$$C_{coh} = \sigma_0 / \left(2\sqrt{(1+\mu')}\right) \tag{5}$$

Table 3. Summary of Experimental Conditions and Results[a]

Run	T (°C)	P_{eff} (MPa)	Strain Rate (x $10^{-5}s^{-1}$)	Peak Strength or σ at 2% (MPa)	σ at 5% (MPa)	Stress Evolution
GB 1	400	100	1	915	910	S
GB 2	500	100	1	230	276	H
GB 3	600	100	1	150	200	–
GB 4	600	70	1	290	235	H
GB 5*	600	50	1	225	–	S
GB 5*	600	70	1	–	225	–
GB 6*	600	100	1	226		H
GB 6*	600	100	0.1		220	–
GB 7*	600	50	1	140	–	H
GB 7*	600	50	0.33	–	150	H
GB 8*	650	200	1	112	–	H
GB 8*	650	250	1	–	130	H
GB 9	700	100	1	169	265	H
GB 10	800	100	1	50	54	H
GB11*	800	100	1	70	90	H
GB 12*	800	100	1	40	–	S
GB 12*	800	100	5	–	45	–
GB13	900	100	0.1	35	50	H
GB14	900	100	1	55	50	H
GB 15*	900	100	1	20	–	H
GB 15*	900	100	5	–	25	–
GB 16	600	300	1	101	160	H
GB 17	700	300	1	67	110	H
GB 18	750	300	1	46	70	H
GB 19	800	300	1	48	60	H
GB 20	900	300	1	40	45	H
GB 21*	900	300	1	35	–	H
GB 21*	900	300	5	–	35	–
GFB 1	400	100	1	1026	–	S
GFB 2	600	100	1	872	–	S
GFB 3	700	100	1	550	–	S
GFB 4	800	100	1	473	–	S
GFB 5*	800	100	1	450		S
GFB 5*	800	100	0.5	–	248	–
GFB 6	900	100	1	414	215	S
GFB 7	600	300	1	704	–	S
GFB 8	700	300	1	646	692	–
GFB 9	800	300	1	506	485	S
GFB 10	800	300	1	520	590	H
GFB 11	850	300	1	386	450	–
GFB 12*	900	300	1	274	288	–
GFB 13*	950	300	1	123	–	–
GFB 13*	950	300	0.5	–	80	–

[a]Column 1: Experiment run. Runs with an asterisk: strain rate stepping tests. Column 3: Effective confining pressure. $P_{eff} = P_c - P_p$, P_{eff} is the effective pressure. P_c is the confining pressure. P_p is the pore fluid pressure. Column 5: For stress–strain curves showing weakening, this corresponds to the peak stress. For strain hardening curves, we report $\sigma_1 - \sigma_3$ at 2%. Column 6: we report $\sigma_1 - \sigma_3$ at 5% of effective strain. Column 7: Mode. W: Strain weakening after σ_{max} and localization; H: Strain hardening.

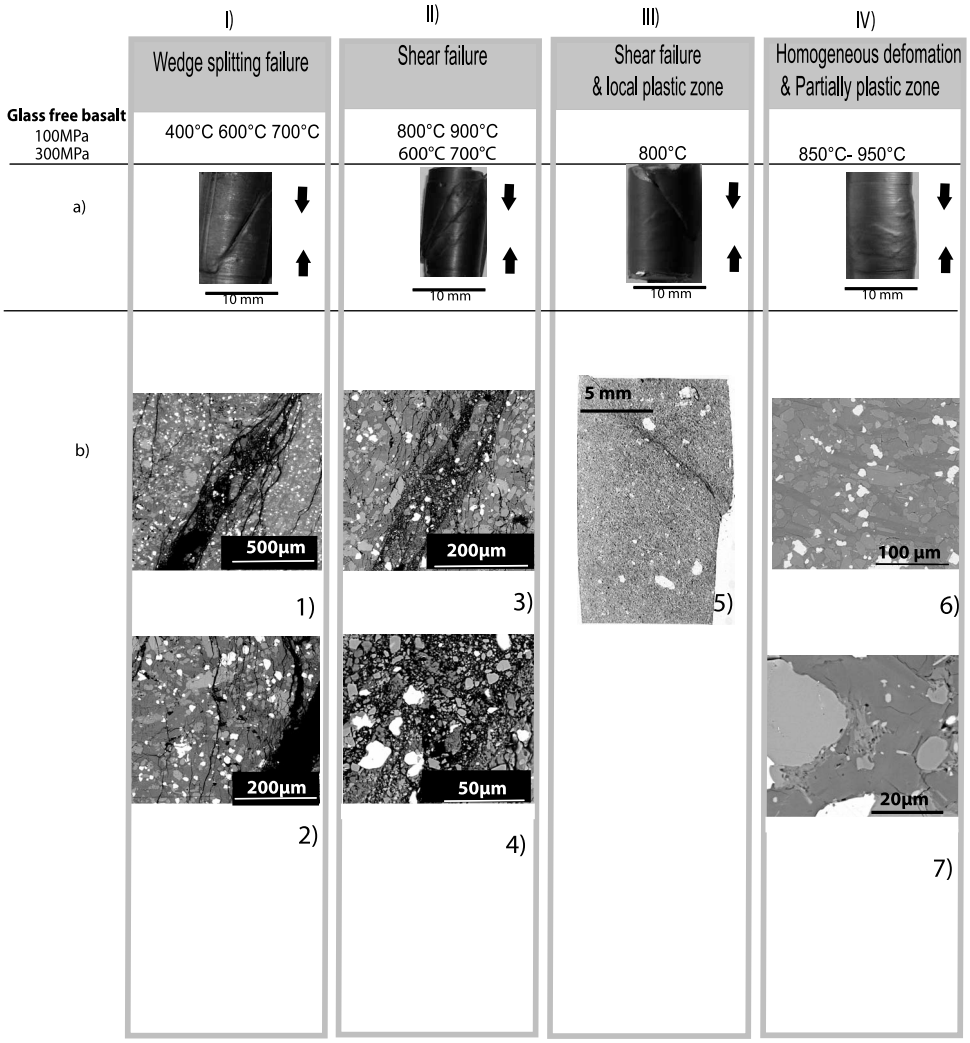

Figure 5. (a) Photographs post-run jacketed GFB sample. (b) Microstructures of several deformed GFB samples of basalt on thin sections. Image 5 shows optical plane-polarized light micrograph; images 1–4 and 6–8 show Backscattered Scanning Electron microphotograph.

At high T and P_c, when cataclasis can be neglected, dislocation creep may be important and is often represented by a steady state power law:

$$\dot{\varepsilon} = A.\sigma^n.\exp(-Q/RT) \quad (6)$$

where A is a material constant, *n*, the stress exponent, Q, the activation energy, R, the gas constant. All of these constitutive laws are rough generalizations that neglect many possibly important state variables, including fluid chemistry, pore geometry, and evolution of the structure of the solid [*Evans*, 2005].

[33] The transition from one mechanism to another may be gradual. As P_c and T increase, cataclasis is suppressed, and intracrystalline defect migration is enabled. Thus, the aggregate rock strength becomes less sensitive to confining pressure and more sensitive to temperature and strain rate. Pressure sensitivity is usually very low when rock strength is less than the confining pressure, an empirical observation called the Goetze criterion [*Kohlstedt et al.*, 1995]. In the region in σ, P_c space between Byerlee's rule and the Goetze criterion, deformation in dry compact rocks is often distributed, and strain accommodated by a combination of cataclasis and intracrystalline mechanisms.

[34] A similar framework for the change in failure mode from macroscopically localized, brittle fracture to ductile, non-localized flow can be formulated [*Heard*, 1960; *Evans et al.*, 1990; *Paterson and Wong*, 2005]. Here, we use the term "ductile" simply to denote the capacity of a sample to deform without localized faulting [cf. *Paterson and Wong*, 2005; *Rutter and Neumann*, 1995], not to imply isochoric strain, or that any particular deformation mechanism operates. Notice that this definition is a macroscopic characterization of the aggregate deformation, as are stress-strain measurements.

[35] Localized brittle failure in compact rocks without melt typically occurs under conditions of T and P_c, where the peak strength, given by the Coulomb failure criterion, is greater than that required to cause slip on an optimally oriented fracture, as given by Byerlee's rule (see equation (2) and Figure 6). The distinction between brittle and ductile deformation modes may be quite complicated, particularly

for multiphase materials, because the transition from one mode to another may be gradual, and because different phases might exhibit different failure modes at the same time. All of the remarks above, regarding both mechanism and mode, are great simplifications and rough generalizations. But, they may be used as a framework to analyze more complex mechanical behavior, like the semi-brittle deformation observed in these basalt samples.

6.2. Deformation Mode and Mechanisms in Basalt at High T and P

[36] Changes in the deformation mode roughly correlate with the stress-strain behavior in both suites of samples, as predicted by the generalized framework. In glassy samples, localization was accompanied either by strain weakening or by deformation at nominally constant stress (500–800°C, 100 MPa); while distributed deformation was always accompanied by strain-hardening. In the glass-free basalt, localization always corresponded to strain weakening, whereas distributed deformation occurred at constant stress. As expected, the degree of localization and grain comminution in both basalts decreased with increasing pressure and temperature. For GB, at 400°C, 100 MPa, localization was intense, whereas at 500°C < T < 800°C and 100 MPa, rupture occurred along broader zones of crushed grains. In the GFB, as P and T increased, the failure mode changed from wedge splitting (400–600°C, 100 MPa), to shear rupture (700–900°C, 100 MPa, or 600–800°C, 300 MPa), finally to homogeneous flow (800°C, 300 MPa). It is sometimes difficult to identify the relative activity of various deformation mechanisms. Characteristic microstructural fingerprints of intracrystalline mechanisms are not evident from the optical and SEM observations used here. Brittle mechanisms are less circumspect. For example, cataclasis was certainly involved in the deformation of the GB sample at 600°C 300 MPa. In those samples that contain a glass phase, it is possible, if not likely, that the glass might be mobile at the higher temperatures, but not leave microstructural evidence.

[37] There were, however, significant differences from the generalized framework shown by the mechanical behavior of both sets of samples. For these experimental conditions, the strength of basalt was affected by strain rate, $\dot{\varepsilon}$, finite strain, ε, absolute temperature, T, and confining pressure, P_c, and none of the end-member constitutive laws accurately describes all of the data for either the GB or GFB samples, which deformed by mixed mechanisms in a semi-brittle regime [*Paterson and Wong*, 2005]. Also, notice that our axial compression tests were limited to strains <15%. Thus, one does not know if weakening, hardening, or a steady state would occur at higher strains. Moreover, precise yield points marking the departure from linear behavior were not always obvious. Finally, the initial, presumably elastic domain of the stress-strain curves varied from one experiment to another. Given these complexities, we explicitly describe the effect of each physical parameter on strength.

6.3. Effect of Confining Pressure

[38] The brittle-ductile transition in basalt is favored by increases in P_c and T. For the GB samples at 100 MPa, brittle failure occurs at 400 to 700°C, while ductile behavior only occurs at 800–900°C. At 300 MPa, ductile behavior begins at 600°C. GFB samples are brittle at 400–900°C and 100 MPa, and at 600–700°C and 300 MPa; ductile behavior occurred between 800 and 950°C at 300 MPa. For the GFB, at 100 MPa, deformation localized at all temperatures, also at the highest temperature (900°C), i.e., localized failure persisted to higher temperatures than predicted by Byerlee's rule (Figure 6). At P_C = 300 MPa, the transition to ductility occurs within the semi-brittle field, but still at higher temperatures than expected (800°C to 850°C). It is important to mention that the transition in mode will probably depend on strain rate, which in our experiments was limited to the range 10^{-4} -10^{-6} s^{-1}. For GB samples, the change of strength with increased P_c was small or even negative. Strengths at a strain rate of 10^{-5} s^{-1}, 400 < T < 600°C, and P_c = 100 MPa were large: from 900 to 250 MPa. When P_c = 300 MPa, strengths never exceeded 100 MPa. At these conditions, all strengths were well below the confining pressure and deformation was distributed, consistent with the Goetze criterion.

[39] In Figure 7 we plot the sliding stress, at 5% permanent strain, after stress drops had occurred, and, presumably, when strain had localized along a rupture plane (Table 3). Notice that the sliding stress for both GB and GFB samples depends strongly on effective pressure at all temperatures. The friction (sliding) coefficient was determined from pressure dependence of steady state sliding strength (characterized by a constant value of differential stress) (Figure 7a). The coefficient of friction at a strain of 5% is similar for GB and GBF samples.

6.4. Temperature Dependence

[40] In the brittle (localized) domain, the peak fracture strength of the glassy basalts depends only sensitively on T, except at the lowest temperatures (400°C) where samples were very strong. At 100 MPa and 600°C, the peak strength is scattered, apparently owing to sample-to-sample variability (Figure 6). Sliding stress values also show scatter of order 50% (Figure 7). For the glass-free samples, both peak strength (Figure 6) and the sliding stress at 5% (Figure 7) showed systematic, but modest, decreases with temperature in the intervals 700°–900°C at 100 MPa and 600°–800°C at 300 MPa $\sim$ (0.5 MPa/°C). GFB samples at 400°C and 600°C and 100 MPa were quite strong (Figure 6). In the ductile (distributed) domain at strain up to 8%, the strength of both GB and GFB samples decreased systematically with the temperature (>20 MPa) (Figures 2 and 6). The temperature dependence of the GFB samples was greater than the GB series (cf. Figure 8), where we plotted the logarithm of strain rate versus the inverse of temperature for P_c = 100 MPa). Q, the activation energies of the GB and GFB are 59 $kJ.mol^{-1}$ $\pm$ 15 and 456 $\pm$ 4 $kJ.mol^{-1}$ respectively (see section 7.2).

6.5. Strain Rate Dependence

[41] In the brittle domain, the peak strength of both GB and GFB samples depended weakly on strain rate (Figures 3 and 9). Notice the marked difference in strain rate sensitivity between samples with localized and distributed deformation, particularly for the glassy samples. GB samples with localized deformation had small or even slightly negative strain rate sensitivity (Figure 9), but their peak strength still decreased with T over the range 600 to 800°C. When strain was distributed, the strain rate sensitivity of strength was much more pronounced, increasing with temperature. The temperature effect was larger for the GFB. Stress-relaxation

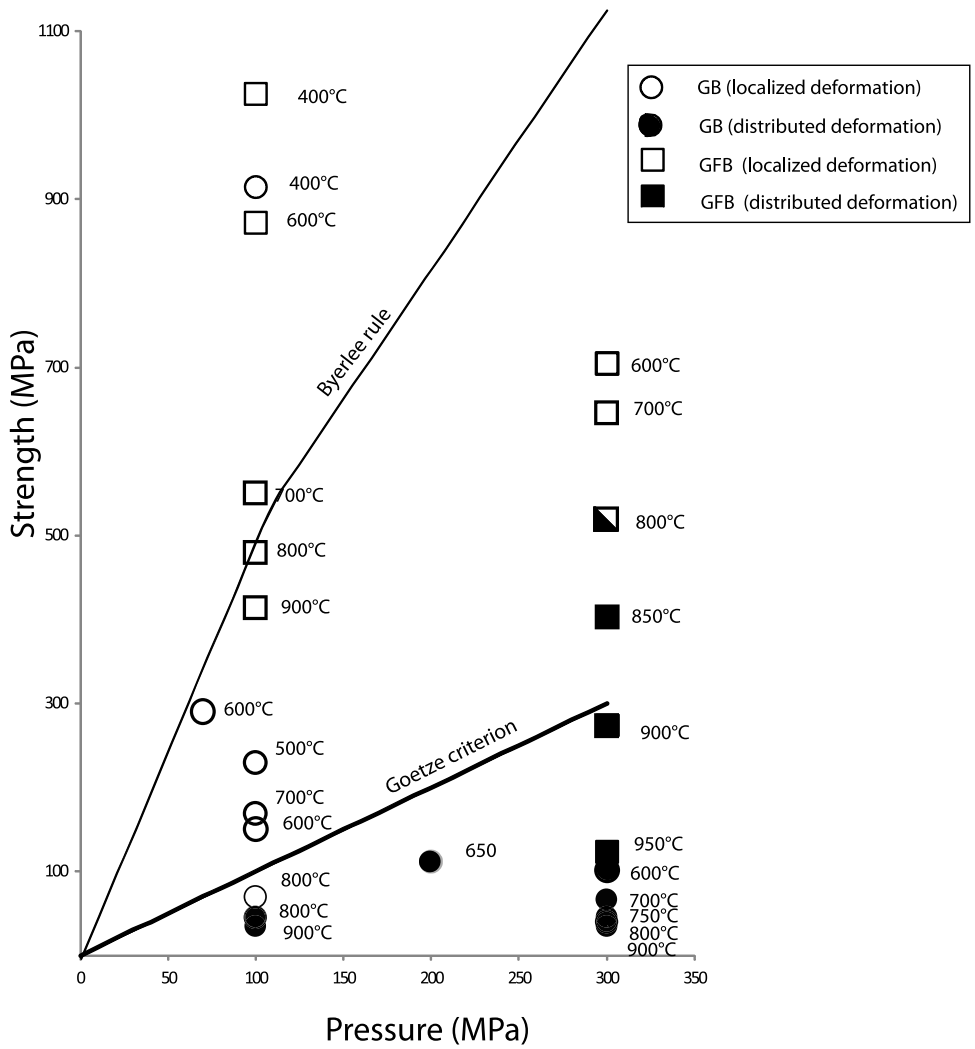

Figure 6. Strength versus pressure for 400°C < T < 950°C. Peak stresses are reported for samples that localized, and the differential stress at 2% strain for samples that showed distributed deformation. Open symbols indicate localized deformation; full symbols had distributed deformation. Byerlee's rule and the Goetze criterion are given as references.

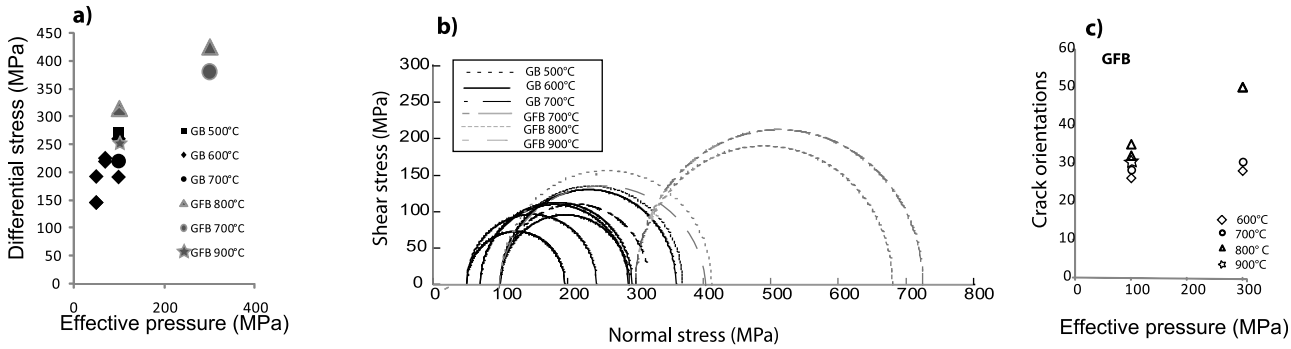

Figure 7. Maximum differential stress increases with effective confining pressure for brittle deformed samples. On the strain-stress curves, the stress value is picked at 2% after stress drop. (a) Linear trend of effective confining pressure versus friction stress at strain rate of 10^{-5} s^{-1}. (b) Mohr circle constructed with the data presented on Figure 3a. The line approximately tangent to the Mohr circles indicates a coefficient of friction $\mu = 0.42$ and C = 34 MPa. (c) Cracks orientations versus pressures for GFB sample.

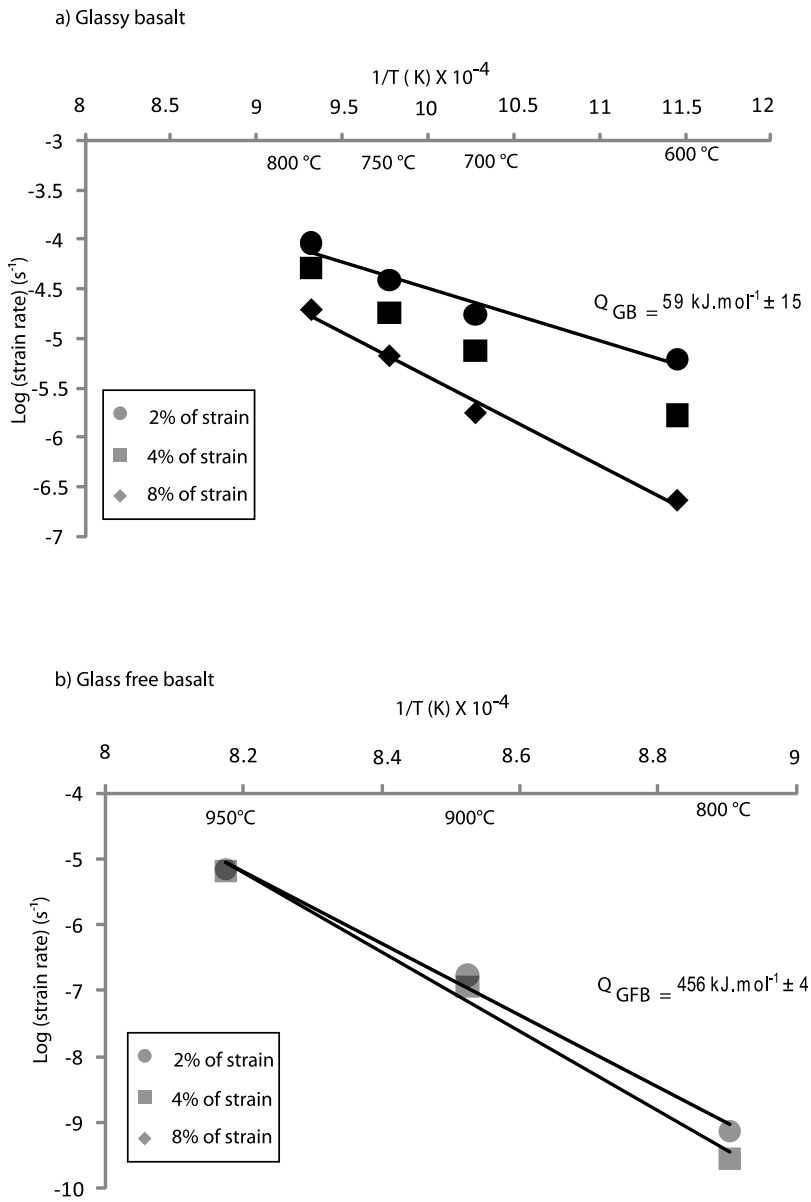

Figure 8. Plots of stress versus the reciprocal temperature at different finite strain. (a) GB sample. (b) GFB sample.

tests generally agree with constant strain rate tests, but both types show scatter, probably reflecting sample heterogeneities and sample-to-sample variability.

6.6. Finite Strain Dependence

[42] The peak strength of the GB sample at 400°C and P_c = 100 MPa and GFB sample at 400°C and 600°C is followed by a load drop and then strain weakening (Figure 2). At 300 MPa, GB samples hardened at all strains and temperature, but the hardening rate systematically decreased from 600 to 750°C, becoming very small at higher T (Figure 2b).

6.7. Tentative Constitutive Laws

6.7.1. Brittle (Localized) Behavior

[43] The peak strength in the localized regime for both GB and GFB samples is only weakly sensitive to strain rate. Similarly, the sliding strength, after the load drop, is insensitive both to strain or strain rate, roughly consistent with the generalized view presented in section 6.1. But, the pressure sensitivity of peak strength, especially of the GB samples is inconsistent with that view. In addition, the glassy basalt strength is temperature sensitive (Figure 9). The friction coefficient was determined from Mohr circles plots measured at $\dot{\varepsilon} = 10^{-5}$ s^{-1} (Figure 7b). A linear fit between σ_1–σ_3 and P_{eff} gives a slope $\mu' = 1.3$ and $\sigma_o = 106$ MPa. From equation (4), the coefficient of friction, $\mu = 0.42$ and cohesive strength $C_{oh} = 34$ MPa. The fracture angle characteristic of these parameters is of 33° to the compression direction, which corresponds to our observations on GFB at 100 MPa (600°C–900°C) and 300 MPa (600° and 700°C) (Figure 7c). These values are lower than those suggested by *Byerlee* [1978] ($\tau = 50 + 0.6.\sigma n$), but agree with previous

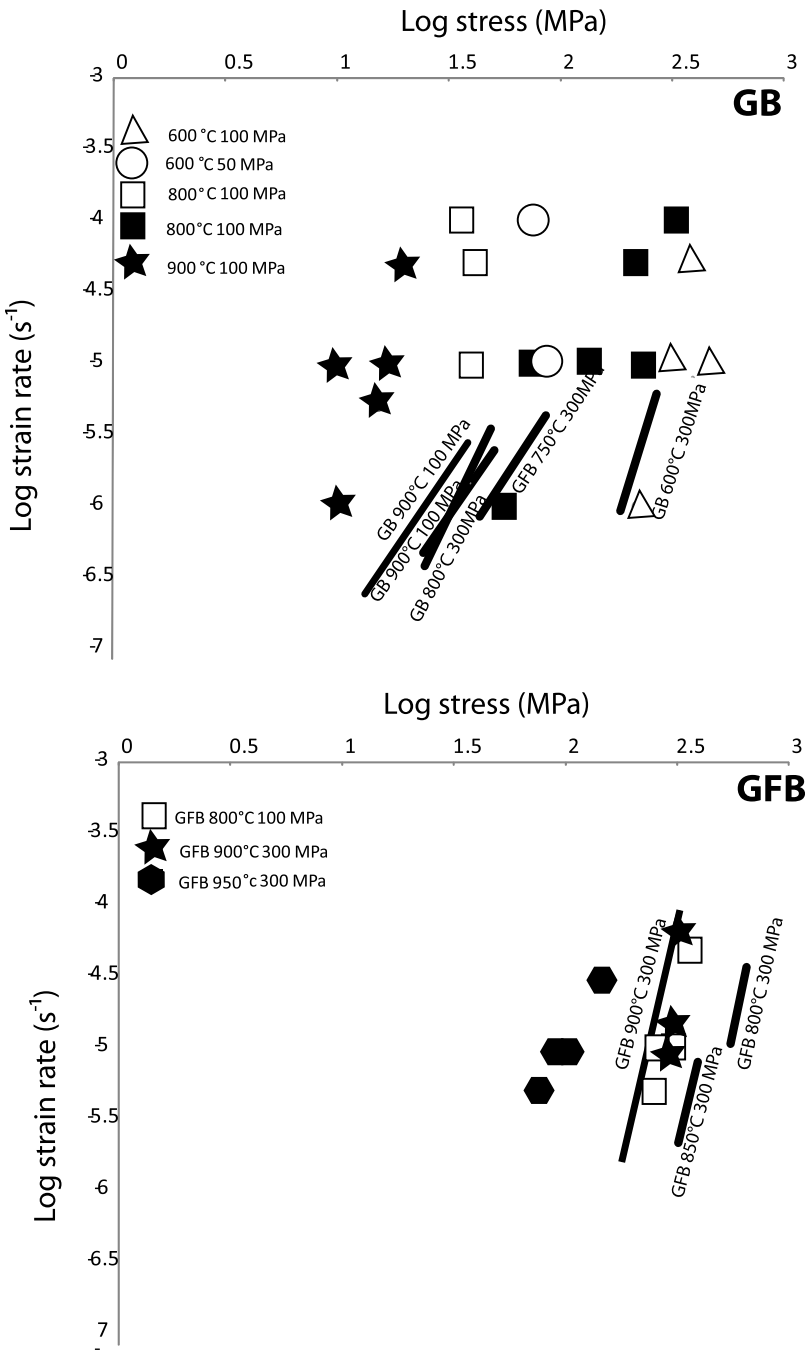

Figure 9. Plots of log strain rate versus log stress. (top) GB sample, (bottom) GFB sample. Open symbols correspond to localized deformation. Full symbols correspond to distributed deformation. Symbols are strain rate stepping tests. Solid lines are stress relaxation tests.

studies on various volcanic rocks at low temperature ($0.43 < \mu < 0.6$) [*Rocchi et al.*, 2003].

6.7.2. Ductile (Distributed) Behavior

[44] The behavior in the ductile field is more difficult to describe, probably owing to the operation of both cataclastic and intracrystalline deformation mechanisms or to redistribution of melt. Failing a detailed mechanical description of semi-brittle flow, we analyze strength in the ductile regime by computing effective parameters using the power law (equation (6)). Using this constitutive law will be an approximate lower bound of the actual rock strength, in the case of work hardening, or an upper bound in the case of strain softening, even without extrapolation. It is clear that a more accurate constitutive law is necessary to describe the basalt behavior at conditions different than those tested here.

[45] To determine the apparent n, Q, and A for equation (6), we used only results between 700°C and 900°C and at confining pressure of 300 MPa for glassy samples. For GFB, we used data only between 850°C and 950°C at a confining pressure of 300 MPa. The strain rate dependence was determined from strain rate-steps and stress relaxations that were applied in most runs (Figures 3 and 9; Table 3).

Table 4. Creep Data From Previous Studies on Diabases and Present Study

	A (MPa $^{-n}$ s^{-1})	n	Q (kJ mole^{-1})
Shelton and Tullis [1981]	?	3.4	250
Caristan [1982] (Maryland diabase)	6.1E-2	3.1	270
Kirby and Kronenberg [1984]	1.6E-05	6.4	444
Mackwell et al. [1998] (Columbia diabase)	1.9 ± 1.1E02	4.7 ± 0.6	488 ± 35
Mackwell et al. [1998] (Maryland diabase)	8.0 ± 4.0	4.7 ± 0.8	482 ± 25
Hacker and Christie [1992] (675°C–775°C)	5.3 ± 1.0E-09	5.4 ± 0.2	263 ± 20
Hacker and Christie [1992] (825°C–875°C)	1.1 ± 0.1E-05	3.3 ± 0.1	175 ± 30
Dimanov and Dresen [2005] (dislocation creep - dry conditions)	2.7E-12 (+2.6E-10/−2.6E-12)	4.1 ± 0.2	723 ± 52
Dimanov and Dresen [2005] (diffusion creep - dry conditions)	6.7E04 (+1.1E06/−6.4E04)	1.0	496 ± 34
GB (present study)	1.3 ± 0.8E-09	3.7 ± 0.6	59 ± 15
GFB (present study)	6.1 ± 2.2E08	3.6 ± 0.6	456 ± 4

Additional creep tests were performed at constant stresses of 70 MPa and 100 MPa and confining pressures of 300 MPa. Stress exponent *n* was determined from linear regression of log (stress) versus log (strain rate) at each temperature (Figure 9).

[46] For GB, the stress exponent (n) ranges from 3.1 to 4.3. For the GFB, n ranges from 3.0 to 4.2. The activation energy was determined from a least squares fit of log (stress) versus 1/T at a given strain rate, or by correcting the strain rates to a given constant stress of 100 MPa at each temperature and fitting the logarithm strain rate versus inverse temperature (Figure 8). The strength at 5% was used unless strength continued to evolve. Then, the activation energy was also calculated at different strains.

[47] For glassy samples, the activation energy is weakly dependent on finite strain and was 59 ± 15 kJ/mol, a relatively low value when compared to diabase or feldspar rocks without melt. For glass-free basalt, the activation energy is independent of the finite strain. The fact that activation energy and stress exponents do not evolve during experiments for GFB and only slightly for GB samples suggests that the relative activities of the various deformation processes evolve slowly over this strain interval. However, there is a considerable difference in the apparent activation energies of the GB and GFB: 59 kJ.mol^{-1} ± 15 and 456 ± 4 kJ.mol^{-1} respectively.

[48] Combining average values for apparent *n* and *Q*, the following strain rate laws are calculated (*cf* Table 4):

$$\text{GB}: \dot{\varepsilon} = \left(1.3 \pm 0.8 * 10^{-9}\right)\sigma^{(3.7\pm0.6)} \cdot \exp^{((-59,0\pm15)/\text{RT})}$$

$$\text{GFB}: \dot{\varepsilon} = \left(6.1 \pm 2.2 * 10^{8}\right)\cdot\sigma^{(3.6\pm0.6)} \cdot \exp^{((-456,0\pm4)/\text{RT})}$$

where the stress is in MPa, the activation energy in kJ/mol and the pre-exponential term in MPa^{n}s^{-1}. The large uncertainty of the pre-exponential term reflects sample-to-sample variability and heterogeneity, but also owes to the explicit complexity of the actual mechanisms.

7. Discussion: Strengths of Glassy and Glass-Free Basalts

[49] In the brittle field, the kinematics of the deformation modes of the glassy and non-glassy basalts are quite similar: In the localized regime, cataclastic rupture planes developed with clear evidence of grain comminution. Peak strengths were reached within a few per cent strain, followed by rapid weakening. Thereafter, sliding occurred along the rupture planes; during this phase, both glassy and glass-free rocks had roughly the same friction coefficient, 0.4. However, the peak fracture strength and the sliding strength of the glassy basalts were always lower than those of that were glass free. When glass was present, the transition from brittle to ductile modes occurred at a lower pressure. In the ductile domain, the presence of glass was associated with reduced strength, and there was also a large reduction in the apparent activation energy. In contrast, the stress-sensitivity of strain rate, *n*, was the same for both rocks. Notice that the two sample suites differed in composition only by the amount of glass. Below, we compare the current results to previously published studies of basalt and diabase, assess the impact of the presence of glass on ductile deformation, and discuss the effect of petrology on strength.

7.1. Mechanical Tests on Glass-Free Basalts

[50] Early mechanical tests were conducted on non-glassy diabases in a solid-medium apparatus by *Shelton and Tullis* [1981], in a gas apparatus by *Caristan* [1982], and on synthetic gabbros in a gas apparatus by *Dimanov and Dresen* [2005] and *Dimanov et al.* [2007]. The *Caristan* [1982] tests were constant strain rate experiments on Maryland diabase at P_c = 450 MPa, T = 1000°C and $2.10^{-3} < \dot{\varepsilon} < 4.10^{-6}$. Deformed samples had a combination of brittle and plastic microstructures. It was later discovered that these rocks initially contained a small concentration of alteration minerals, which dehydrated at high temperature, liberated water, formed a small amount of melt, weakened the samples, and promoted stress drops [*Evans et al.*, 1990; *Mackwell et al.*, 1998]. When the diabases were dried at high temperatures, no melt formed during the deformation tests, and they were strengthened [*Mackwell et al.*, 1998]. Creep tests on dried Maryland and Columbia diabases at 900°C < T < 1050°C, P_c = 500 MPa, and strain rate from $10^{-7} < \dot{\varepsilon} < 10^{-5}$ s^{-1} indicate the operation of dislocation creep. Strength from the flow laws for diabase at $\dot{\varepsilon} = 10^{-5}$ s^{-1} are plotted versus temperature [*Caristan*, 1982; *Kirby and Kronenberg*, 1984; *Mackwell et al.*, 1998] in Figure 11. For comparison, data for GB and GFB are also given.

[51] The diabase strength measured by *Caristan* [1982] and *Mackwell et al.* [1998] are higher than that of GFB by a factor of three at 800°C, and six at 1100°C. The stress exponent in all three studies are similar, but our activation energy is slightly lower than those found earlier (Table 4). Small strength variations might be explained by differences

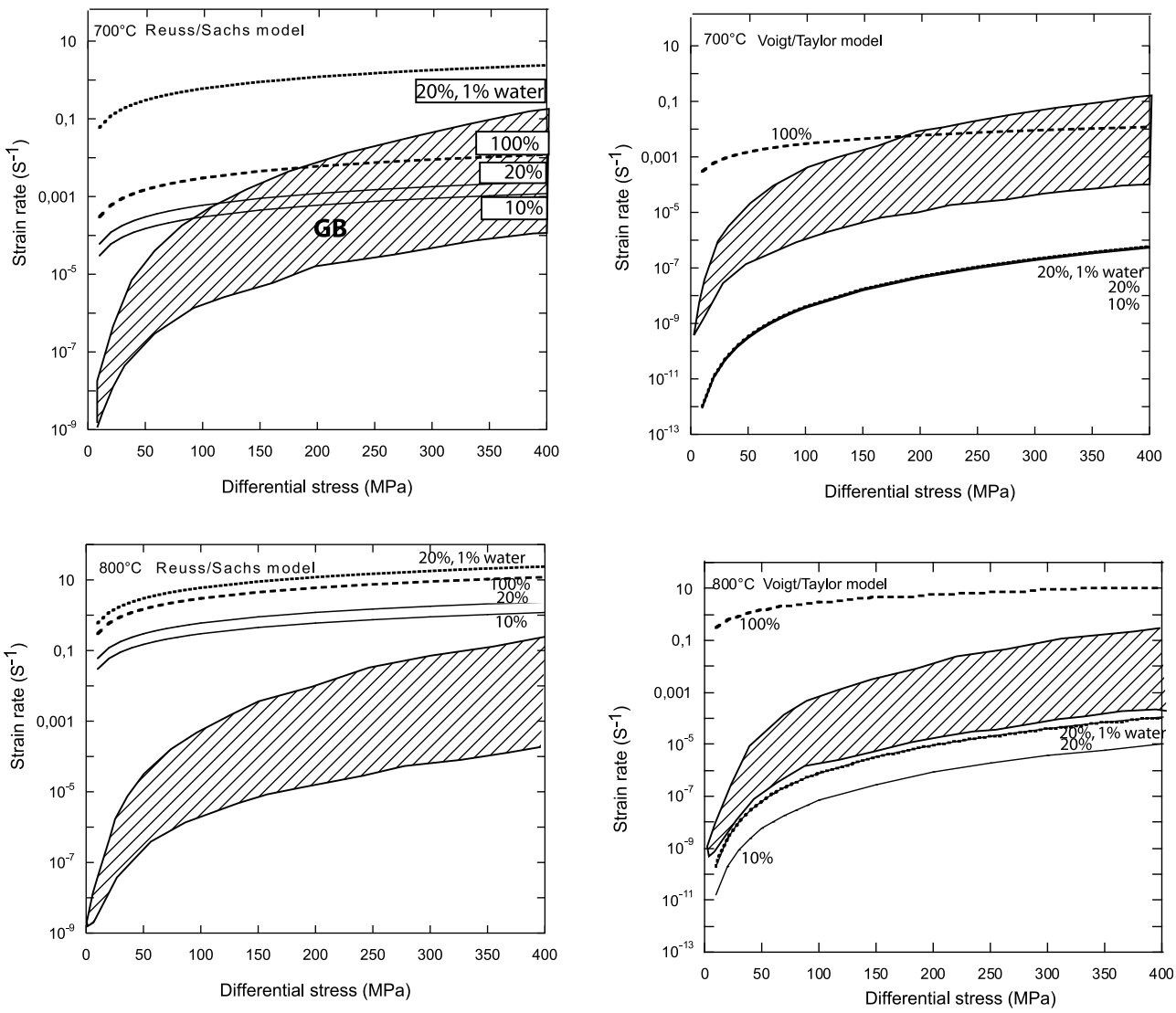

Figure 10. Two components models (glass and basalt) calculated in series and parallel at temperature of 700°C and 800°C for 10%, 20%, 100% of dry melt, 20% of hydrated (1% of water) melt. Glass rheology is derived from *Whittington et al.* [2001]. Basalt rheology is derived from GFB power flow law. GB rheology is given as reference (shaded area).

in the petrology, but the modal and chemical composition of Maryland diabase and the GFB are quite similar. The grain size and crystal shapes of clinopyroxene and plagioclase in the GFB groundmass are also different: groundmass plagioclase sizes are heterogeneous and average of 50 μm in length. Augite and plagioclase are frequently xenomorphic. In Maryland diabase, plagioclase size is homogeneous and ≈200 μm. Augite and plagioclase appear pseudo-automorphic [*Caristan*, 1982]. However, high-temperature dislocation creep in feldspar and pyroxene is usually affected only weakly by grain size [*Rybacki and Dresen*, 2004; *Dimanov and Dresen*, 2005; *Dimanov et al.*, 2011]. Chemical effects, including changes in water or oxygen fugacity, can influence both the strength of the crystalline phases, especially pyroxene, and the viscosity of the melt [*Giordano et al.*, 2008]. Accessory phases are one way that volatile fugacities can be buffered, and we note that the oxide content of Maryland diabase is ∼1%, but is 10% in GFB.

7.2. Mechanical Tests on Glassy Basalts

[52] *Hacker and Christie* [1992] (HC) deformed a glassy plagioclase-rich basalt at T between 675 and 875°C, P_c = 1 GPa, and strain rates of 10^{-4}–10^{-7} s^{-1} in a solid-medium apparatus; those workers cast their results in terms of a power law creep equation with no explicit dependence on melt content (equation (4)). Our apparent stress exponents at 800 < T < 900°C are similar to theirs, but our apparent activation energy (59 ± 15 KJ/mol^{-1}) is about 3 times smaller (175 ± 30 KJ/mol^{-1}) (Table 4). There are several other differences between their samples and ours. The glass content was 10–15% in HC; and 15–25% in GB. The glass composition was rhyolitic for HC; and phonolitic for GB. The plagioclase HC basalt was ductile at all conditions, whereas our samples deformed in both localized and ductile modes. Deformation in HC occurred by a combination of cracking, dislocation glide, and glass flow. Cracks formed

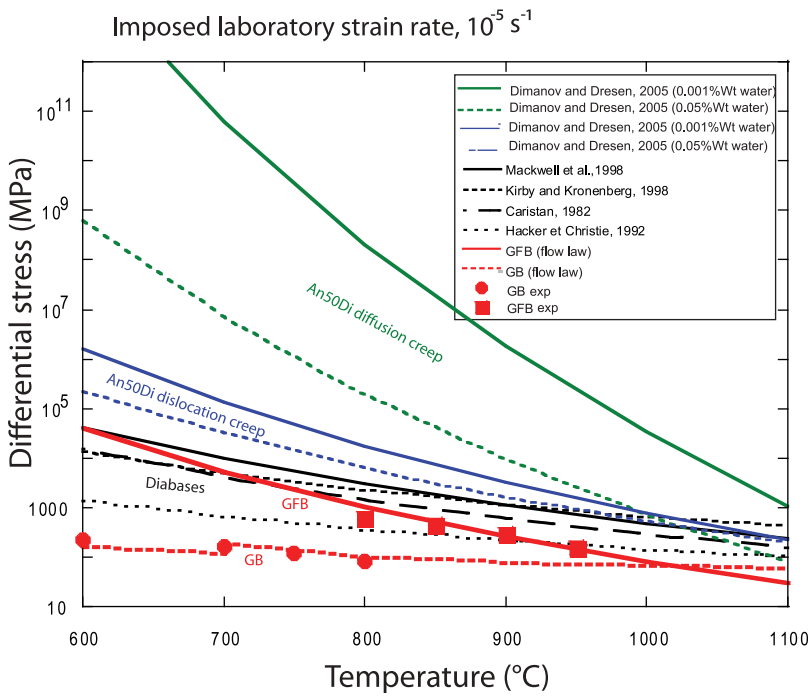

Figure 11. Plot of differential stress versus temperature. Stresses are calculated for strain rate of 10^{-5} s^{-1} using a flow law for diabases (black curves) [*Mackwell et al.*, 1998; *Caristan*, 1982; *Shelton and Tullis*, 1981] and flow law of GB and GFB (red curves). Experimental points are also given (red points). Flow laws for dislocation creep (green curves) and flow law for diffusion creep (blue curves) of 50%plagioclase-50%clinopyroxene aggregates with 0.005%Wt water (solid line) and 0.0075%Wt water (dashed line) [*Dimanov and Dresen*, 2005] are given as references. Flow law for diffusion creep of plagioclase-clinopyroxene aggregates [*Dimanov and Dresen*, 2005] is given for ~3 μm grain size with a grain size exponent m = 3.

into a network of micro-faults inclined at 40–50° to the compression axis, a similar geometry to that observed in our samples.

[53] Many previous studies in a variety of partially molten rocks, indicate that aggregate strength depends on the melt fraction, ϕ_m, the distribution of the melt [*Arzi*, 1978; *Hirth and Kohlstedt*, 1995; *Scott and Kohlstedt*, 2006; *Van der Molen and Paterson*, 1979; *Dimanov et al.*, 1998, 2000], and the capacity of the melt to migrate [*Dell'Angelo and Tullis*, 1988; *Holtzman et al.*, 2003; *Renner et al.*, 2000]. For example, in partially molten peridotite at T > 1200°C, where melt is well-connected at almost all degrees of partial melting, strength decreases by 2.5 orders of magnitude over the interval, $0 < \phi_m < 0.20$ [*Scott and Kohlstedt*, 2006]. The apparent stress sensitivity, n, and activation energy, Q, in the dislocation creep regime do not depend on melt content, suggesting that the effect of ϕ_m can be incorporated into the flow low as a separable function:

$$\dot{\varepsilon} = A'\sigma^n \exp(-\alpha\phi_m) \exp\left(\frac{-Q}{RT}\right) \quad (7)$$

where A′ and α are empirical material constants, and n and Q are the same as for peridotite without melt. For the basalts, under the conditions of our experiments, apparent n values for GB and GFB samples are similar, but the apparent activation energies are quite different, a complication not admitted by equation (7).

[54] Melt migration is also an important aspect for the mechanical behavior. At low strain rates or if melt is well connected, migration will promote ductile deformation and may favor inter-granular flow or diffusion creep. At high strain rates, or when poorly connected, the melt may be effectively undrained, thus, promoting brittle deformation [*Ko et al.*, 1997; *Renner et al.*, 2000]. We did not directly observe deformation or migration of the glassy phase. However, EBSD results in the GB sample deformed at 900°C suggest that deformation was associated with a weak disorganization of the initial crystalline fabric, and that clinopyroxene crystals throughout the sample rotated with respect to the compression axis. The lack of evidence of dislocation creep is also consistent with rigid rotation. Thus, the deformation kinematics might be described, at least tentatively, as relatively large rigid crystals rotating in soft matrix of micro- to nano-sized crystals and glass, a description corresponding to SEM images.

[55] In the interval, $\phi_m \approx 0.20$–0.40, the strength of partially molten rock evolves from that characteristic of a solid with liquid inclusions, to that of a liquid with solid inclusions [*Arzi*, 1978; *Van der Molen and Paterson*, 1979; *Riley and Kohlstedt*, 1991; *Rutter and Neumann*, 1995; *Barboza and Bergantz*, 1998; *Renner et al.*, 2000; *Rosenberg and Handy*, 2005]. The glass content of the glassy samples, between 15 and 25%, is near the lower bound of this rheological transition, suggesting that a simple flow law

considering a single mechanism may not be adequate to describe the mechanical behavior of basalt.

[56] As a first small step to include a second mechanism, we treat the rock as an aggregate composed of two separate crystalline and glass phases, using the well-known mixing laws [*Clyne and Withers*, 1993]:

$$\frac{1}{\dot{\varepsilon}_{GB}} = \left(\frac{v}{\dot{\varepsilon}_{Glass}}\right) + \left(\frac{1-v}{\dot{\varepsilon}_{GFB}}\right) \tag{8}$$

$$\dot{\varepsilon}_{GB} = v\,\dot{\varepsilon}_{Glass} + (1-v)\,\dot{\varepsilon}_{GFB} \tag{9}$$

where v is the volume fraction of glass in the mixture, and $\dot{\varepsilon}_{GB}$, $\dot{\varepsilon}_{Glass}$, and $\dot{\varepsilon}_{GFB}$ are the average strain rates for the glassy aggregate, the glass phase, and crystalline component, respectively.

[57] When the creep process in one phase is dependent on each other the processes of other phase they are said to be sequential, in such a case each mechanism participates for a different increment of time. Since the strain contribution of each phase must be identical to maintain aggregate integrity the respective contributions are weighted by their volume fractions as given in equation (8). The physical configuration of such a two-phase system is often idealized as a slab model with parallel layers of the two phases with a homogeneous stress field, sometimes referred to as the Reuss (elastic) or Sachs (plastic) model. The slower process dominates the strain rate, but not the necessarily the strain (and microstructure), as the slower process must operate and produce strain, so that the faster one can operate in a sequential manner. In contrast, when the creep processes in each phase operate independently each of them contributes to the strain over the entire time increment considered, so that the volume fraction weighted strain rates are additive as shown in equation (9). In this case the strain field in the idealized two-slab is homogeneous and fastest mechanism dominates the strain rate, this type of behavior is called the Voigt (elastic) or Taylor (plastic) model. The Voigt/Taylor behavior should have significant impact on the microstructure.

[58] For strength in crystalline phase we use mechanical results for glass-free basalt (GFB). The EPMA analyses of the glass in the GB samples show that its composition is close to a hydrated phonolitic melt with 1–2% of water. Thus, the viscosity of phonolitic melt have been used [*Whittington et al.*, 2001]. At our experimental temperatures, the viscosity for a dry phonolitic melt varies between 10^7 and 10^{21} Pa.s, and between 10^5 and 10^{13} Pa.s for a hydrated phonolitic melt [*Whittington et al.*, 2001]. Strengths for the two mixing models were calculated at 700°C and 800°C, for basalt with dry melt fraction (ϕ_m) of 10%, 20%, and for basalt with melt hydrated with 1% of water of ϕ_m = 20%. The results are plotted in Figure 10 along with data for the GB tests and for phonolitic melts. None of the models matches the GB data completely, but at 700°C, the GB strengths are intermediate between the Voigt/Taylor and Reuss/Sachs models for samples with ϕ_m = 20%, hydrated with 1% water. At 800°C, the GB rheology is closer to the Voigt/Taylor with ϕ_m = 20%, dry or wet. These comparisons suggest that the water content of melt might be an important aspect of the rheology of the glassy samples. Second, the differences in activation energy between GB and GFB samples suggest that a process other than dislocation creep, probably having to do with melt migration or deformation, accommodates part of the deformation. In addition to changes in melt viscosity, the strength may be affected by other factors, including changing melt connectivity, local elevations or depression of melt pressure, changes in the proportion or size of crystalline phases within the melt, or fugacity of water. Clearly, a more sophisticated model involving more information on the microstructure would provide better physical constraints on the mechanics of the deformation.

7.3. The Impact of Microstructure and Petrology on Mechanical Behavior

[59] During the tests, biotite and nepheline grew, replacing glass and magnetite in all GB samples deformed at high pressure (300 MPa). Neo-mineralization affected only about 10% of the glass fraction of each sample, and neo-crystals were less than 10 μm in length. In parallel, glass chemistry evolves during experiments; in particularly the glass dehydrates, which implies changes of its viscosity, and hence potential effects on the mechanical response of the glassy basalt itself. Experiments of longer duration are needed to study the influence of metamorphism on the deformation process. However, the crystallization of quartz and mica during Hacker and Christie's experiments did not seem to affect the mechanical behavior of that glassy basalt. Although we also have no direct evidence that metamorphism affects deformation mechanisms in our samples, it seems possible that hardening might result from changing melt chemistry or reduction in permeability caused by changes in the crystal fraction of the amorphous phase.

[60] Grain size difference between GB and GFB has a potential impact on deformation at high temperature. Both samples have approximately the same clinopyroxene grain size, but GB plagioclase grain size (50–200 μm), is twice as large as GFB plagioclase grain size (20–80 μm). At high-temperature, dislocation creep in feldspar is usually affected only weakly by grain size, however grain boundary diffusion-creep is significantly affected by grain size distribution [cf. *Dimanov et al.*, 1999, 2003, 2007, 2011; *Dimanov and Dresen*, 2005].

[61] On the Figure 11, the differential stress versus temperature is plotted for strain rate of 10^{-5} s^{-1} using the flow laws of GB and GFB, and flow laws for diabases [*Mackwell et al.*, 1998; *Caristan*, 1982; *Shelton and Tullis*, 1981]. Flow laws for dislocation creep and flow law for diffusion creep of 50% plagioclase 50% clinopyroxene aggregates [*Dimanov and Dresen*, 2005] are given as a reference. Flow law for diffusion creep of plagioclase-clinopyroxene aggregates [*Dimanov and Dresen*, 2005] is given for 3 μm grain size with a grain size exponent m = 3, [see *Dimanov and Dresen*, 2005, equation 1].

[62] The mechanical behavior of GB and GFB at our experimental temperature and strain rate are not compatible with the diffusion creep regime (even for very small grain size), as shown in Figure 11. GFB mechanical behavior is compatible with the dislocation creep regime. Small differential stress difference between GFB and plagioclase-clinopyroxene aggregates of *Dimanov and Dresen* [2005], might be explain by difference in petrology (aggregates do not contain oxide, plagioclase is anorthite and not labradorite…), and in porosity (aggregates porosity is <1%). GB

sample present an additional complexity due the presence of glass. Stress exponents ($3 < n < 4.2$), for both GB, and GFB samples, could be indicative of deformation dominated by dislocation creep processes. We therefore postulate that plagioclase grain size difference between GB and GFB samples cannot explain their difference in mechanical behavior. However, grain boundary diffusion-controlled process can be a concomitant or co-operational mechanism for grains of very small size and may contribute to deformation, in particular in presence of a liquid phase, as suggested *Dimanov and Dresen* [2005]. Further microstructural observations must be done to quantify the importance of the grain boundary diffusion-controlled process on the deformation of GB and GFB.

[63] Oxide accessory phases might also be important. The first sign of plastic deformation in GBF sample was the elongation of oxides, parallel to the shear zone boundaries, which occurred at about 700°C. At this temperature, plagioclases and clinopyroxene deform by combination of microcracking and heterogeneous cracking [*Kronenberg and Shelton*, 1980]. Yet, little is known about the role of Fe-Ti-oxides during shear zone deformation. *Agar and Lloyd* [1997] have suggested that in nature, magnetite deforms by diffusion creep at T up to 550 to 650°C. So, Fe-Ti-oxides behave as highly ductile phases at low temperature [*Muller and Siemes*, 1972]. Thus, high concentrations of Fe-Ti-oxide in shear zones might significantly reduce basalt strength.

8. Implication for Oceanic Crust

[64] The strength of oceanic crust, largely composed of basaltic rocks, is a function of temperature, pressure, fluid chemistry, lithology, melt and glass chemistry, and melt volume fraction. Glass is unlikely to persist for long times at depth [*Staudigel and Hart*, 1983], but is sometimes found at dykes or the margins of magma flows [*Ross*, 1983; *Thy et al.*, 1985; *Fisk et al.*, 1996].

[65] The brittle to ductile transition in rocks has often been described as a parameter that can influence the absolute permeability value and the porosity topology. The BDT may be an indicator of the maximum depth and temperature at which hydrothermal fluids may circulate.

[66] Indeed, in low porosity rocks, laboratory measurements indicate that, for both brittle failure and cataclastic flow, dilatancy (porosity increasing with strain) and permeability increase. Permeability increases monotonically till localized brittle failure occurs [*Zoback and Byerlee*, 1975; *Peach and Spiers*, 1996; *Zhu and Wong*, 1997; *Mitchell and Faulkner*, 2008; *De Paola et al.*, 2009]. For example, the permeability of Westerly granite increased by a factor of 3 when the sample was stressed to 80% of the peak fracture strength [*Zoback and Byerlee*, 1975]. In the cataclastic regime, measurements on halite [*Peach and Spiers*, 1996; *Stormont and Daemen*, 1992], on Carrara marble, and hot pressed calcite [*Zhang et al.*, 1994] all indicate rapid increases of permeability with the accumulation of several percent strain. Microstructural analyses led to the interpretation that the large increase in permeability in the brittle domain is due to a large connected network of intragranular and intergranular microfractures [*Brace and Byerlee*, 1967; *Zoback and Byerlee*, 1975; *Zhang et al.*, 1994; *Moore and Lockner*, 1995; *Peach and Spiers*, 1996; *Siddiqi et al.*, 1997; *De Paola et al.*, 2009].

[67] In the ductile domain (distributed deformation), low porosity rocks, can be associated with minor dilatancy or compaction depending of the deformation mechanism. For the cataclastic creep mechanism, in calcite [*Zhang et al.*, 1994]; in quartz-calcite aggregate [*Siddiqi et al.*, 1997]; in anhydrite [*De Paola et al.*, 2009], the ductile deformation is associated with minor dilatancy that leads to a small increase in permeability with increasing finite strain, until it is stabilized to a fixed value when a percolation threshold is reached. *De Paola et al.* [2009] state that the permeability value is lower than the permeability attained immediately prior to failure in the brittle mode.

[68] For others deformation mechanisms such as hydrostatic compaction [*Bernabé et al.*, 1982; *David et al.*, 1994], shear enhance compaction [*Zhang et al.*, 1994], ductile deformation can decrease the pore space and reduce the permeability. Little is known regarding the effect on fluid-transport properties in rocks undergoing ductile deformation by crystal plastic or diffusion flow mechanisms [see *Fischer and Paterson*, 1989]. When rocks are deformed in the triaxial configuration at elevated temperatures and large effective pressures, permeability and porosity tend to be reduced with strain, although the response depends critically on the state of drainage of the pore fluid [*Fischer and Paterson*, 1989]. In undrained mechanical tests on partially molten peridotite, melt-rich lenses develop with spacing that is related to the permeability of the rock matrix and the viscosity of the melt [*Holtzman et al.*, 2003]. Permeability was not measured directly, but microstructure suggests that the melt rich lenses have a much higher in permeability, but that the lenses evolve and move throughout the aggregate.

[69] We can make some simplified first order estimates of the depth of the brittle/ductile transition in the basaltic crust to constrain the maximum depth at which hydrothermal fluids circulate. Even with this first order approach it requires large extrapolations in strain rate of our laboratory data to the mechanical behavior in natural situations. Here we suggest a simple rheological model based only on GBF data, fully recognizing limitations the simple model. The friction law of GB and GFB and power law for GFB were used to calculate the strength as a function of depth, assuming a strain rate of 10^{-14} s^{-1} and two different thermal gradients suggested for the oceanic crust at the axial Icelandic rift [*Foulger*, 1995] (Figure 12).

[70] In addition to assuming that the large extrapolation in strain rate is valid, one must also assume constant strain rate throughout the section, and that the entire oceanic crust consists of basalt of the same chemistry, that strength in the localized regime is determined by the stress to cause slip on a optimally oriented fault, that the rocks are effectively drained, and that local heterogeneities in fluid pressure do not exist. Even so, the validity of the extrapolation strongly depends on the accuracy of the determination of μ, n, and Q in the constitutive relations. For GFB sample the error of Q is ± 4 kJ/mol, which corresponds to an error of ± 200 m in depth. The standard deviation of $n \pm 0.6$ for GB and GFB causes an error of about 600 m on the depth of the brittle to ductile transition, we obtained similar values to that for Columbia and Maryland diabase given by *Mackwell et al.* [1998].

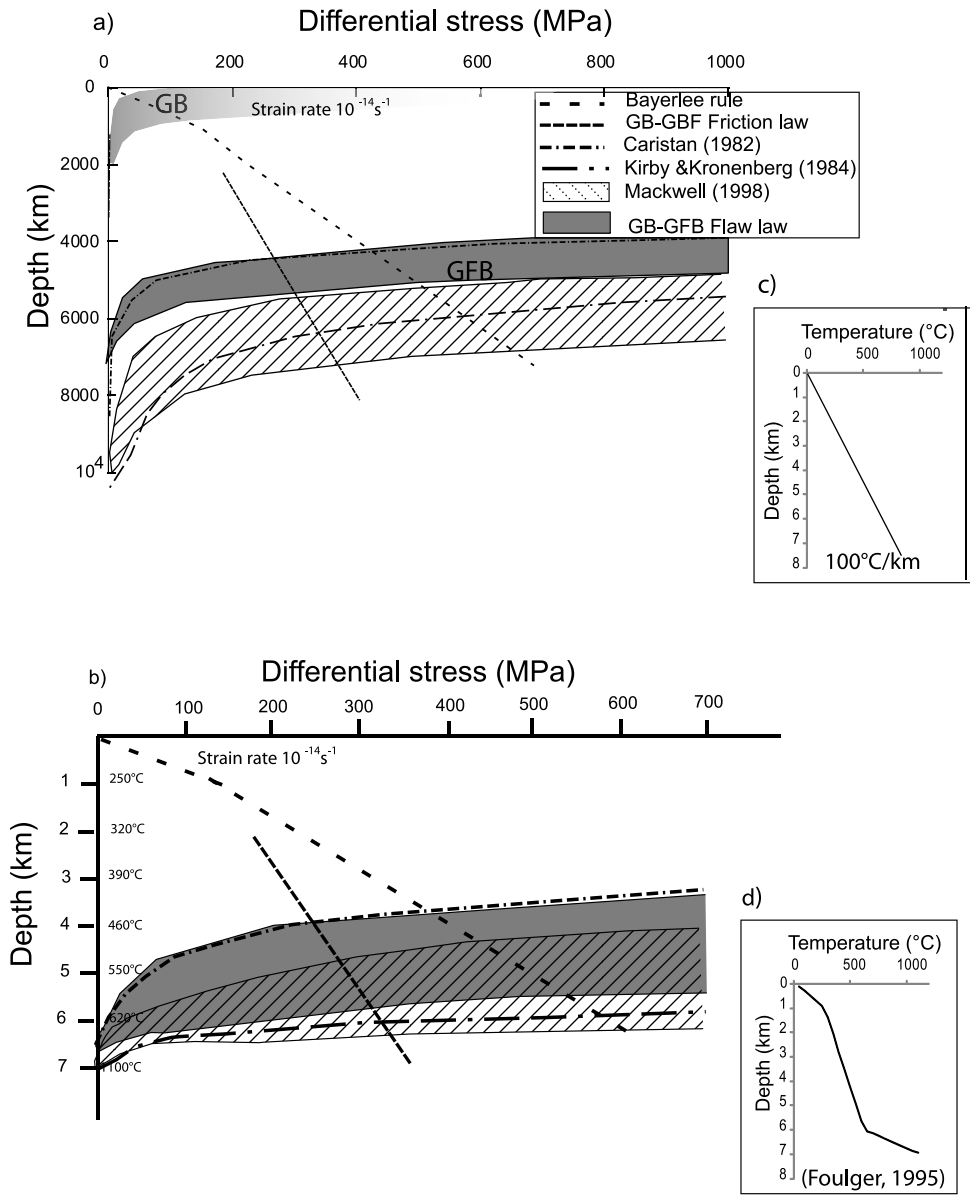

Figure 12. (a and b) Differential stress versus depth profile for a typical Iceland crust at the rift axis. (c) Strain rate of 10^{-14} s^{-1} was used in all calculation. (d) Thermal profile used in calculation [*Foulger*, 1995].

[71] With these assumptions we estimate that glass free basalt may deform in the brittle field up to 550 ± 100°C at 10^{-14} s^{-1}. In Figure 12a, GB rheology is also given for comparison.

[72] If these extrapolations are correct, hydrothermal fluids might circulate, at least transiently, through the oceanic basaltic crust down to 5 to 7 km depth. Clearly, supercritical fluids might be expected at these depths within the volcanic rift zone (Figure 12). This estimate is coherent with the lower limit of the Icelandic seismogenic zone, which seems to be associated with the isotherm for 650 ± 100°C [*Fridleifsson and Elders*, 2005].

[73] Some geological observations also agree with this model. Several petrological studies based on ophiolite petrology and on characterizations of the oceanic crust suggest that high temperature metamorphism (500–700°C) in diabase and gabbros can be linked to hydrothermal circulation e.g., Diabase in at Hole IODP 1256D are altered in the amphibolite facies [*Wilson et al.*, 2006]. Gabbros from Hess deep (Site IODP 894) show also alteration at temperatures of 700–750°C [*Manning et al.*, 1996]. Sheeted dikes complex at Troddos Ophiolite show hydrothermal alteration of 550 −750°C [*Gillis*, 2002].

[74] It is important to emphasize that, because of the high temperature, large values of effective lithostatic pressure are not likely to persist, and that reductions in permeability owing to mineral crystallization or compaction of the solid matrix. Once again, the physical and chemical state of the pore fluids, whether aqueous or silicate, will be an extremely important parameters, and these will quite probably evolve. Additional tests are needed, particularly experiments where permeability and volumetric strain could be measured

independently. Long-term experiments with reactive pore fluids are also desirable; in order to investigate the modifications of pore space induced by metamorphic reaction coupled with deformation [*Heap et al.*, 2011].

[75] Based on the same assumptions as before (strain rate extrapolation of GFB sample), we estimate that the linear viscosity of the lower Iceland crust, at 10 Km depth, 800–1000°C, and geological strain rate of 10^{-14} s^{-1}, is between 6.10^{19}–4.10^{18} Pa s. The result is coherent with ground displacements observations associated with large earthquake in the southern Iceland crust, from which *Jónsson* [2008] made a model estimate the lower crust viscosity at 10–20 km depth of between 4.10^{18} and 2.10^{19} Pa s.

9. Conclusions

[76] Brittle to ductile transition is one of the most important variables controlling the permeability of rock and consequently the fluid flow in hydrothermal systems. New experimental data obtained on two low porosity basalts performed at a constant strain rate of 1×10^{-5} s^{-1} and a confining pressure of 100 MPa and 300 MPa, pore pressure of 30 to 70 MPa and temperature between 400°C and 950°C are presented in this work. It constitutes one of the first experimental studies of basalt deformation under brittle and ductile deformation mode at oceanic crustal conditions.

[77] Mechanical observations at 10^{-5} s^{-1} show the following:

[78] 1. The rocks are brittle and dilatant up to 700–800°C.

[79] 2. At higher temperatures and effective pressures the deformation mode becomes macroscopically ductile, i.e., deformation is distributed throughout the sample.

[80] 3. The brittle to ductile transition strongly depends on the lithology. Several percent of glass does strongly influence the pressure and temperature at the brittle to ductile transition occurs.

[81] 4. In the brittle field, strength is consistent with a Mohr-Coulomb failure criterion with an internal coefficient of friction of 0.42 for both samples.

[82] 5. In the ductile field, strength is strain rate- and temperature-dependent and both samples were characterized by the same stress exponent in the range $3 < n < 4.2$. In contrast activation energies $Q_{GB} = 59 \pm 15$ KJ/mol and $Q_{GFB} = 456 \pm 4$ KJ/mol respectively are very different and strongly dependent on the glass volume fraction.

[83] 6. The extrapolation of these mechanical results to geological strain rates indicate that basaltic rocks may deform in the brittle field to temperature up to ~550 ± 100°C. The association of these data with the observed temperature gradients in volcanic zones in Iceland indicate that hydrothermal fluids might circulate, at least transiently, through the oceanic basaltic crust down to 4 to 6 km. At these depths and temperatures, fluids are in the supercritical state. Such fluids have been recently recognized to be of important scientific and industrial interest, in particular for geothermal energy. For instance, Iceland Deep Drilling Project (IDDP) whose main objective is to characterize the physical properties of the deep reservoir in order to produce supercritical hydrous fluids from drillable depth in Iceland [*Fridleifsson and Elders*, 2005; *Massiot et al.*, 2010], predicts that the extraction of supercritical fluids may enhance by a factor of ten the electrical power of conventional geothermal power plants [*Albertsson et al.*, 2003].

[84] Finally, the present experiments were done for a limited set of strain rates and pressures. Because the rocks are deforming by both cataclastic and plastic processes, the exact scaling of strength with effective lithostatic pressure, pore fluid pressure, and deformation rate needs further clarification. When pore fluids are present, chemical and mechanical interactions with the rock matrix may cause important modifications to the geometry of the pore space that will undoubtedly influence both the rock strength and the transport properties of the rocks.

[85] **Acknowledgments.** We thank Fabrice Barou for assistance with EBSD measurements with CrystalProbe at the CNRS-INSU-UM2 Geosciences EBSD facility. Anne-Lise Faivre is thanked for calorimetric measurements. Christophe Nevado and Doriane Delmas are thanked for excellent thin section preparation of very difficult specimens. We are grateful for financial support from EEC geothermal research program HiTI, directed by Ragnar Asmundsson, as well as from ADEME and BRGM. This manuscript was significantly improved by the pertinent reviews by A. Dimanov and M. Heap.

References

Agar, S. M., and G. E. Lloyd (1997), Deformation of Fe-Ti oxides in gabbroic shear zones from the MARK area, *Proc. Ocean Drill. Program Sci. Results*, *153*, 123–141.

Ágústsson, K., and O. G. Flovenz (2005), The Thickness of the Seismogenic Crust in Iceland and its Implications for Geothermal Systems, paper presented at World Geothermal Congress 2005, Int. Geotherm. Assoc., Antalya, Turkey.

Albertsson, A., J. O. Bjarnason, T. Gunnarsson, C. Ballzus, and K. Ingason (2003), The Iceland Deep Drilling Project: Fluid handling evaluation and utilization, paper presented at International Geothermal Conference IGC-2003, Int. Energy Agency, Reykjavik.

Alt, J. C., et al. (1996), Hydrothermal alteration of a section of upper oceanic crust in the eastern equatorial Pacific: A synthesis of results from Site 504 (DSDP legs 69, 70, and 83, and ODP legs 111, 137, 140, and 148), *Proc. Ocean Drill. Program Sci. Results*, *148*, 417–434, doi:10.2973/odp.proc.sr.148.159.

Arzi, A. (1978), Critical phenomena in the rheology of partially melted rocks, *Tectonophysics*, *44*, 173–184, doi:10.1016/0040-1951(78)90069-0.

Avé Lallement, H. G. (1978), Experimental deformation of diopside and websterite, *Tectonophysics*, *48*, 1–27, doi:10.1016/0040-1951(78)90083-5.

Barboza, S. A., and G. W. Bergantz (1998), Rheological transitions and the progress of melting of crustal rocks, *Earth Planet. Sci. Lett.*, *158*, 19–29, doi:10.1016/S0012-821X(98)00047-8.

Bernabé, Y., W. F. Brace, and B. Evans (1982), Permeability, porosity and pore geometry of hot pressed calcite, *Mech. Mater.*, *1*, 173–183, doi:10.1016/0167-6636(82)90010-2.

Bjornsson, A. (2008), Temperature of the Icelandic crust: Inferred from electrical conductivity, temperature surface gradient, and maximum depth of earthquakes, *Tectonophysics*, *447*(1–4), 136–141.

Borg, I. Y., and H. C. Heard (1969), Mechanical twinning and slip in experimental deformed plagioclase?, *Contrib. Mineral. Petrol.*, *23*, 128–135.

Borg, I. Y., and H. C. Heard (1970), Experimental deformation of plagioclases, in *Experimental and Natural Rock Deformation*, edited by P. Paulitsch, pp. 375–403, Springer, New York.

Brace, W. F., and J. D. Byerlee (1967), Recent experimental studies of brittle fracture in rocks, in *Failure and Breakage of Rock: Proceedings of the Eighth Symposium on Rock Mechanics Held at the Univ. of Minnesota September 15–17, 1966*, edited by C. Fairhurst, pp. 58–81, Am. Inst. of Min. Metall. and Pet. Eng., New York.

Byerlee, J. D. (1978), Friction of rocks, *Pure Appl. Geophys.*, *116*, 615–626, doi:10.1007/BF00876528.

Caristan, Y. (1982), The transition from high temperature creep to fracture in Maryland diabase, *J. Geophys. Res.*, *87*, 6781–6790, doi:10.1029/JB087iB08p06781.

Chen, Y., and W. J. Morgan (1990), A non-linear rheology model for mid-ocean ridge axis topography, *J. Geophys. Res.*, *88*, 4183–4214.

Clyne, T. W., and P. J. Withers (1993), *An Introduction Metal Matrix Composites*, Cambridge Univ. Press, Cambridge, U. K., doi:10.1017/CBO9780511623080.

David, C., T.-F. Wong, W. Zhu, and J. Zhang (1994), Laboratory measurement of compaction induced permeability change in porous rocks: Implication for the generation and maintenance of pore pressure excess in the crust, *Pure Appl. Geophys.*, *143*, 425–456.

Dell'Angelo, L. N., and J. Tullis (1988), Experimental deformation of partially melted granitic aggregates, *Geology*, *6*, 495–515.

Dell'Angelo, L. N., J. Tullis, and R. A. Yund (1987), Transition from dislocation creep to melt-enhanced diffusion creep in *fine-grained* granitic aggregates, *Tectonophysics*, *139*, 325–332, doi:10.1016/0040-1951(87)90107-7.

De Paola, N., D. R. Faulkner, and C. Collettini (2009), Brittle versus ductile deformation as the main control properties of low-porosity anhydrite rocks, *J. Geophys. Res.*, *114*, B06211, doi:10.1029/2008JB005967.

Dimanov, A., and G. Dresen (2005), Rheology of synthetic anorthite-diopside aggregates: Implications for ductile shear zones, *J. Geophys. Res.*, *110*, B07203, doi:10.1029/2004JB003431.

Dimanov, A., G. Dresen, and R. Wirth (1998), High-temperature creep of partially molten plagioclase aggregates, *J. Geophys. Res.*, *103*(B5), 9651–9664, doi:10.1029/97JB03742.

Dimanov, A., G. Dresen, X. Xiao, and R. Wirth (1999), Grain boundary diffusion creep of synthetic anorthite aggregates: The effect of water, *J. Geophys. Res.*, *104*(B5), 10,483–10,497, doi:10.1029/1998JB900113.

Dimanov, A., G. Dresen, and R. Wirth (2000), The effect of melt distribution on the rheology of plagioclase rocks, *Tectonophysics*, *328*, 307–327, doi:10.1016/S0040-1951(00)00214-6.

Dimanov, A., M. P. Lavie, G. Dresen, J. Ingrin, and O. Jaoul (2003), Creep of polycrystalline anorthite and diopside, *J. Geophys. Res.*, *108*(B1), 2061, doi:10.1029/2002JB001815.

Dimanov, A., E. Rybacki, R. Wirth, and G. Dresen (2007), Creep and strain-dependent microstructures of synthetic anorthite - diopside aggregates, *J. Struct. Geol.*, *29*(6), 1049–1069, doi:10.1016/j.jsg.2007.02.010.

Dimanov, A., G. Dresen, and J. Raphanel (2011), Newtonian flow of heterogeneous synthetic gabbros at high strain: Grain sliding, ductile failure, and contrasting local mechanisms and interactions, *Eur. J. Mineral.*, *23*(3), 303–322, doi:10.1127/0935-1221/2011/0023-2110.

Edmond, J. M., K. L. Van Damm, R. E. MacDuff, and C. I. Measures (1982), Chemistry of hot springs on the East Pacific Rise and their effluent dispersal, *Nature*, *297*, 187–191, doi:10.1038/297187a0.

Elderfield, H., and A. Schultz (1996), Mid-ocean ridge hydrothermal fluxes and the chemical composition of the ocean, *Annu. Rev. Earth Planet. Sci.*, *24*, 191–224.

Evans, B. (2005), Creep constitutive laws for rocks with evolving structure, in *High Strain Zones*, edited by D. Bruhn and L. Burlini, *Geol. Soc. Spec. Publ.*, *245*, 329–346, doi:10.1144/GSL.SP.2005.245.01.16.

Evans, B., J. T. Fredrich, and T.-F. Wong (1990), The brittle to ductile transition in rocks: Recent experimental and theoretical progress, in *The Brittle-Ductile Transition in Rocks*, *Geophys. Monogr. Ser*, vol. 56, edited by A. G. Duba et al., pp. 1–20, AGU, Washington, D. C., doi:10.1029/GM056p0001.

Fischer, G. J., and M. S. Paterson (1989), Dilatancy during rock deformation at high temperatures and pressures, *J. Geophys. Res.*, *94*(B12), 17,607–17,617, doi:10.1029/JB094iB12p17607.

Fischer, G. J., and M. S. Paterson (1992), Measurement of permeability and storage capacity in rocks during deformation at high temperature and pressure, in *Fault Mechanics and Transport Properties of Rocks, Int. Geophys.*, *51*, 213–252.

Fisk, M. R., and A. W. McNeill, D. A. H. Teagle, H. Furnes, and W. Bach (1996), Data report: Major-element chemistry of Hole 896A glass, *Proc. Ocean Drill. Program Sci. Results*, *148*, 483–487.

Fontaine, F. J., M. Rabinowicz, and J. Boulègue (2001), Permeability changes due to mineral diagenesis in fractured crust: Implications for hydrothermal circulation at mid-ocean ridges, *Earth Planet. Sci. Lett.*, *184*, 407–425, doi:10.1016/S0012-821X(00)00332-0.

Fontaine, F. J., M. Cannat, and J. Escartin (2008), Hydrothermal circulation at slow-spreading mid-ocean ridges: The role of along-axis variations in axial lithospheric thickness, *Geology*, *36*(10), 759–762, doi:10.1130/G24885A.1.

Foulger, G. R. (1995), The Hengill geothermal area, Iceland: Variation of temperature gradients deduced from the maximum depth of seismogenesis, *J. Volcanol. Geotherm. Res.*, *65*, 119–133, doi:10.1016/0377-0273(94)00088-X.

Fridleifsson, G. O., and W. A. Elders (2005), The Iceland Deep Drilling Project: A search for deep unconventional geothermal resources, *Geothermics*, *34*, 269–285, doi:10.1016/j.geothermics.2004.11.004.

Frost, H. J., and M. F. Ashby (1982), *Deformation-Mechanism Maps*, Pergamon, Oxford, U. K.

Gillis, K. M. (2002), The root zone of an ancient hydrothermal system exposed in the Troodos Ophiolite, Cyprus, *J. Geol.*, *110*, 57–74, doi:10.1086/324205.

Giordano, D., J. K. Russell, and D. B. Dingwell (2008), Viscosity of magmatic liquids: A model, *Earth Planet. Sci. Lett.*, *271*, 123–134, doi:10.1016/j.epsl.2008.03.038.

Goetze, C., and W. F. Brace (1972), Laboratory observations of high-temperature rheology of rocks, *Tectonophysics*, *13*, 583–600, doi:10.1016/0040-1951(72)90039-X.

Hacker, B. R., and J. M. Christie (1992), Experimental deformation of a glassy basalt, *Tectonophysics*, *200*, 79–96.

He, C., Z. Wang, and W. Yao (2007), Frictional sliding of gabbro gouge under hydrothermal conditions, *Tectonophysics*, *445*, 353–362, doi:10.1016/j.tecto.2007.09.008.

Heap, M. J., P. Baud, P. G. Meredith, S. Vinciguerra, A. F. Bell, and I. G. Main (2011), Brittle creep in basalt: Implications for time-dependent volcano deformation, *Earth Planet. Sci. Lett.*, *307*, 71–82.

Heard, H. C. (1960), Transition from brittle to ductile flow in Solnhofen limestone as a function of temperature, confining pressure, and interstitial fluid pressure rock deformation, *Mem. Geol. Soc. Am.*, *79*, 193–226.

Hirose, T., and N. W. Hayman (2008), Structure, permeability, and strength of a fault zone in the footwall of an oceanic core complex, the central dome of the Atlantis Massif, Mid-Atlantic Ridge. 30°N, *J. Struct. Geol.*, *30*(8), 1060–1071, doi:10.1016/j.jsg.2008.04.009.

Hirth, G., and D. L. Kohlstedt (1995), Experimental constraints on the dynamics of the partially molten upper mantle: 2. Deformation in the dislocation creep regime, *J. Geophys. Res.*, *100*, 15,441–15,449.

Hirth, G., J. Escartin, and J. Lin (1998), The rheology of the lower oceanic crust: Implications for lithospheric deformation at mid-ocean ridges, in *Faulting and Magmatism at Mid-Ocean Ridges*, *Geophys. Monogr. Ser.*, vol. 106, edited by W. Roger Buck et al., pp. 291–323, AGU, Washington, D. C.

Holtzman, B. K., N. J. Groebner, M. E. Zimmerman, S. B. Ginsberg, and D. L. Kohlstedt (2003), Stress-driven melt segregation in partially molten rocks, *Geochem. Geophys. Geosyst.*, *4*(5), 8607, doi:10.1029/2001GC000258.

Johnson, H. P., K. Becker, and R. Von Herzen (1993), Near-axis heat flow measurements on the northern Juan De Fuca Ridge: Implications for fluid circulation in oceanic crust, *Geophys. Res. Lett.*, *20*(17), 1875–1878, doi:10.1029/93GL00734.

Jónsson, S. (2008), Importance of post-seismic viscous relaxation in southern Iceland, *Nat. Geosci.*, *1*, 136–139, doi:10.1038/ngeo105.

Kaban, M. K., Ó. G. Flóvenz, and G. Pálmason (2002), Nature of the crust-mantle transition zone and the thermal state of the upper mantle beneath Iceland from gravity modelling, *Geophys. J. Int.*, *149*, 281–299, doi:10.1046/j.1365-246X.2002.01622.x.

Kirby, S. H., and A. K. Kronenberg (1984), Deformation of clinopyroxenite: Evidence for a transition in flow mechanisms and semi-brittle behavior, *J. Geophys. Res.*, *89*, 3177–3192, doi:10.1029/JB089iB05p03177.

Ko, S. C., D. L. Olgaard, and T. F. Wong (1997), Generation and maintenance of pore pressure excess in a dehydrating system. 1. Experimental and microstructural observations, *J. Geophys. Res.*, *102*(B1), 825–839.

Kohlstedt, D. L., and C. Goetze (1974), Low-stress high-temperature creep in olivine single crystals, *J. Geophys. Res.*, *79*, 2045–2051, doi:10.1029/JB079i014p02045.

Kohlstedt, D. L., B. Evans, and S. J. Mackwell (1995), Strength of the lithosphere: Constraints imposed by laboratory experiments, *J. Geophys. Res.*, *100*(B9), 17,587–17,602.

Kollé, J. J., and J. D. Blacic (1982), Deformation of single-crystal clinopyroxenes: 1. Mechanical twinning in diopside and hedenbergite, *J. Geophys. Res.*, *87*, 4019–4034, doi:10.1029/JB087iB05p04019.

Kollé, J. J., and J. D. Blacic (1983), Deformation of single-crystal clinopyroxenes: 2. Dislocation-controlled flow in hedenbergite, *J. Geophys. Res.*, *88*, 2381–2393, doi:10.1029/JB088iB03p02381.

Koschinsky, A., D. Garbe-Schönberg, S. Sander, K. Schmidt, H. H. Gennerich, and H. Strauss (2008), Hydrothermal venting at pressure-temperature conditions above the critical point of seawater, 5°S on the Mid-Atlantic Ridge, *Geology*, *36*(8), 615–618, doi:10.1130/G24726A.1.

Kronenberg, A. K., and G. L. Shelton (1980), Deformation microstructures in experimentally deformed Maryland diabase, *J. Struct. Geol.*, *23*, 341–352.

Lister, C. R. B. (1980), Heat flow and hydrothermal circulation, *Annu. Rev. Earth Planet. Sci.*, *8*, 95–117, doi:10.1146/annurev.ea.08.050180.000523.

Lockner, D. A. (1995), Rock failure, in *Rock Physics & Phase Relations: A Handbook of Physical Constants*, *AGU Ref. Shelf*, vol. 3, edited by T. A. Ahrens, pp. 127–147, AGU, Washington, D. C., doi:10.1029/RF003p0127.

Lockner, D. A., and T. R. Madden (1991), A multiple-crack model of brittle fracture: 1. Non-time-dependent simulations, *J. Geophys. Res.*, *96*(B12), 19,623–19,642, doi:10.1029/91JB01642.

Lowell, R. P., P. A. Rona, and R. P. Von Herzen (1995), Seafloor hydrothermal systems, *J. Geophys. Res.*, *100*(B1), 327–352, doi:10.1029/94JB02222.

Macdonald, K. C. (1982), "Mid-ocean ridges": Fine scale tectonic, volcanic and hydrothermal processes within the Plate Boundary Zone, *Annu. Rev. Earth Planet. Sci.*, *10*, 155–190, doi:10.1146/annurev.ea.10.050182.001103.

Mackwell, S. J., M. E. Zimmerman, D. L. Kohlstedt, and D. S. Scherber (1998), Experimental deformation of dry Columbia diabase: Implications for tectonics on Venus, in *Rocks Mechanics: Proceedings of the 35th U.S. Symposium*, pp. 207–214, Taylor & Francis, New York.

Manning, C. E., P. E. Weston, and K. I. Mahon (1996), Rapid high-temperature metamorphism of East Pacific Rise gabbros from Hess Deep, *Earth Planet. Sci. Lett.*, *144*, (1–2), 123–132.

Marshall, D. B., and A. C. MacLaren (1977a), Deformation mechanisms in experimentally deformed plagioclase feldspars, *Phys. Chem. Miner.*, *1*, 351–370, doi:10.1007/BF00308845.

Marshall, D. B., and A. C. MacLaren (1977b), The direct observation and analysis of dislocations in experimentally deformed plagioclase feldspars, *J. Mater. Sci.*, *12*, 893–903, doi:10.1007/BF00540970.

Massiot C., P. A. Pezard, and R. Asmundsson (2010), Achievements and ongoing progress of the European HiTI project: High temperature instruments for supercritical geothermal reservoir characterization and exploitation, in *Geothermal: The Energy to Change the World / World Geothermal Congress, 25–30 April 2010*, 12 pp., Indonesian Geotherm. Assoc., Jakarta.

Merlet, C. (1994), An accurate computer correction program for quantitative electron probe microanalysis, *Mikrochim. Acta*, *114–115*, 363–376, doi:10.1007/BF01244563.

Mills, R. A., and H. Elderfield (1995), Rare earth element geochemistry of hydrothermal deposits from the active TAG Mound, 26°N Mid-Atlantic Ridge, *Geochim. Cosmochim. Acta*, *59*, 3511–3524, doi:10.1016/0016-7037(95)00224-N.

Mitchell, T., and D. R. Faulkner (2008), Experimental measurements of permeability evolution during triaxial compression of initially intact crystalline rocks and implications for fluid flow in fault zones, *J. Geophys. Res.*, *113*, B11412, doi:10.1029/2008JB005588.

Moghadam, R. H., C. A. Trepmann, B. Stöckhert, and J. Renner (2010), Rheology of synthetic omphacite aggregates at high pressure and high temperature, *J. Petrol.*, *51*(4), 921–945, doi:10.1093/petrology/egq006.

Moore, D. E., and D. A. Lockner (1995), The role of microcracking in shear-fracture propagation in granite, *J. Struct. Geol.*, *17*, 95–114, doi:10.1016/0191-8141(94)E0018-T.

Moore, G., D. A. Clague, and W. R. Normark (1982), Diverse basalt types from Loihi seamount, Hawaii, *Geology*, *10*, 88–92, doi:10.1130/0091-7613(1982)10<88:DBTFLS>2.0.CO;2.

Morrow, C. A., and D. A. Lockner (1994), Permeability differences between surface-derived and deep drillhole core samples, *Geophys. Res. Lett.*, *21*, 2151–2154, doi:10.1029/94GL01936.

Morrow, C. A., and D. A. Lockner (1997), Permeability and porosity of the Illinois UPH 3 drillhole and a comparison with other deep drillhole rocks, *J. Geophys. Res.*, *102*, 3067–3075, doi:10.1029/96JB03178.

Morrow, C. A., D. Lockner, S. Hickman, M. Rusanov, and T. Rockel (1994), Effects of lithology and depth on the permeability of core samples from the Kola and KTB drill holes, *J. Geophys. Res.*, *99*, 7263–7274, doi:10.1029/93JB03458.

Muller, P., and H. Siemes (1972), Zur Festigkeit und Gefügeregelung von experimentel verformten Magnetitersen, *Neues Jahrb. Mineral Abh.*, *117*, 39–60.

Nara, Y., P. G. Meredith, T. Yoneda, and K. Kaneko (2011), Influence of macro-fractures and micro-fractures on permeability and elastic wave velocities in basalt at elevated pressure, *Tectonophysics*, *503*(1–2), 52–59, doi:10.1016/j.tecto.2010.09.027.

Nelson, C., and D. Giles (1985), Hydrothermal eruption mechanisms and hot spring gold deposits, *Econ. Geol.*, *80*(6), 1633–1639, doi:10.2113/gsecongeo.80.6.1633.

Nicolas, A., D. Mainprice, and F. Boudier (2003), High-temperature seawater circulation throughout crust of oceanic ridges: A model derived from the Oman ophiolites, *J. Geophys. Res.*, *108*(B8), 2371, doi:10.1029/2002JB002094.

Norton, D. L., and R. B. Knapp (1977), Transport phenomena in hydrothermal systems: The nature of porosity, *Am. J. Sci.*, *277*, 913–936, doi:10.2475/ajs.277.8.913.

Pálmason, G., and K. Sæmundsson (1979), Iceland in relation to the Mid-Atlantic Ridge, *Annu. Rev. Earth Planet. Sci. Lett.*, *2*, 25–50.

Paterson, M. S., and T.-F. Wong (2005), *Experimental Rock Deformation - The Brittle Field*, 2nd ed., 347 pp., Springer, Berlin.

Peach, C. J., and C. J. Spiers (1996), Influence of crystal plastic deformation on dilatancy and permeability development in synthetic salt rock, *Tectonophysics*, *256*, 101–128.

Phipps Morgan, W. J., and Y. Chen (1993), Dependence of ridge axis morphology on magma supply and spreading rate, *Nature*, *364*, 706–708, doi:10.1038/364706a0.

Ranero, C. R., T. J. Reston, I. Belykh, and H. Gnibidenko (1997), Reflective oceanic crust formed at a fast-spreading center in the Pacific, *Geology*, *25*(6), 499–522.

Renner, J., B. Evans, and G. Hirth (2000), On the rheological critical melt fraction, *Earth Planet. Sci. Lett.*, *181*(4), 585–594, doi:10.1016/S0012-821X(00)00222-3.

Riley, G. N., Jr., and D. L. Kohlstedt (1991), Kinetics of melt migration in upper mantle-type rocks, *Earth Planet. Sci. Lett.*, *105*(4), 500–521, doi:10.1016/0012-821X(91)90188-N.

Rocchi, V., P. R. Sammonds, and C. R. J. Kilburn (2003), Flow and fracture maps for basaltic rock deformation at high temperatures, *J. Volcanol. Geotherm. Res.*, *120*(1–2), 25–42.

Rosenberg, C. L., and M. R. Handy (2005), Experimental deformation of partially melted granite revisited: Implications for the continental crust, *J. Metamorph. Geol.*, *23*, 19–28, doi:10.1111/j.1525-1314.2005.00555.x.

Ross, M. E. (1983), Chemical and mineralogic variations within four dikes of the Columbia River basalt group, southeastern Columbia Plateau, *Geol. Soc. Am. Bull.*, *94*, 1117–1126, doi:10.1130/0016-7606(1983)94<1117:CAMVWF>2.0.CO;2.

Rutter, E. R., and D. H. Neumann (1995), Experimental deformation of partially molten Westerly granite under fluid-absent conditions, with implications for the extraction of granitic magmas, *J. Geophys. Res.*, *100*, 15,697–15,715.

Rybacki, E., and G. Dresen (2004), Deformation mechanism maps for feldspar rocks, *Tectonophysics*, *382*, 173–187.

Scott, T., and D. L. Kohlstedt (2006), The effect of large melt fraction on the deformation behavior of peridotite, *Earth Planet. Sci. Lett.*, *246*(3–4), 177–187, doi:10.1016/j.epsl.2006.04.027.

Shelton, G., and J. Tullis (1981), Experimental flow laws for crustal rocks, *Eos Trans. AGU*, *62*, 396.

Shimada M., K. Ito, and A. Cho (1989), Ductile behavior of a fine-grained porous basalt at room temperature and pressures to 3 GPa, *Phys. Earth Planet. Inter.*, *55*(3–4), 361–373, doi:10.1016/0031-9201(89)90083-6.

Siddiqi, G., B. Evans, G. Dresen, and D. Freund (1997), Effect of semibrittle deformation on transport properties of calcite rocks, *J. Geophys. Res.*, *102*, 14,765–14,778, doi:10.1029/97JB01038.

Singh, S. C., J. S. Collier, A. J. Harding, G. M. Kent, and J. A. Orcutt (1999), Seismic evidence for a hydrothermal layer above the solid roof of the axial magma chamber at the southern East Pacific Rise, *Geology*, *27*(3), 219–222.

Sleep, N. H., and B. R. Rosendahl (1979), Topography and tectonics of mid-oceanic ridge axes, *J. Geophys. Res.*, *84*, 6831–6839, doi:10.1029/JB084iB12p06831.

Staudigel, H., and S. Hart (1983), Alteration of basaltic glass: Mechanisms and significance for the oceanic crust-seawater budget, *Geochim. Cosmochim. Acta*, *47*, 337–350, doi:10.1016/0016-7037(83)90257-0.

Stein, C., and S. Stein (1994), Constraints on hydrothermal heat flux through the oceanic lithosphere from global heat flow, *J. Geophys. Res.*, *99*, 3081–3095, doi:10.1029/93JB02222.

Stormont, J. C., and J. J. K. Daemen (1992), Laboratory study of gas permeability changes in rock salt during deformation, *Int. J. Rock Mech. Min. Sci.*, *29*, 325–342, doi:10.1016/0148-9062(92)90510-7.

Teagle, D. A. H., J. C. Alt, and A. N. Halliday (1998), Tracing the chemical evolution of fluids during hydrothermal recharge: Constraints from anhydrite recovered in ODP Hole 504B, *Earth Planet. Sci. Lett.*, *155*(3–4), 167–182.

Tolstoy, M., F. Waldhauser, D. R. Bohnenstiehl, R. T. Weekly, and W. Y. Kim (2008), Seismic identification of along-axis hydrothermal flow on the East Pacific Rise, *Nature*, *451*(7175), 181–184.

Tullis, J., and R. A. Yund (1977), Experimental deformation of dry Westerly granite, *J. Geophys. Res.*, *82*, 5705–5718, doi:10.1029/JB082i036p05705.

Tullis, J., and R. A. Yund (1980), Hydrolitic weakening of experimentally deformed Westerly granite and Hale albite rock, *J. Struct. Geol.*, *2*, 439–451, doi:10.1016/0191-8141(80)90005-X.

Tullis, J., and R. A. Yund (1987), Transition for cataclastic flow to dislocation creep of feldspar: Mechanisms and microstructures, *Geology*, *15*, 606–609, doi:10.1130/0091-7613(1987)15<606:TFCFTD>2.0.CO;2.

Tullis, J., and R. A. Yund (1991), Diffusion creep in feldspar aggregates: Experimental evidence, *J. Struct. Geol.*, *13*(9), 987–1000, doi:10.1016/0191-8141(91)90051-J.

Thy, P., C. K. Brooks, and J. N. Walsh (1985), Tectonic and petrogenetic implications of major and rare earth element chemistry of Troodos glasses, Cyprus, *Lithos*, *18*, 165–178.
Van der Molen, I., and M. S. Paterson (1979), Experimental deformation of partially melted granite, *Contrib. Mineral. Petrol.*, *70*, 299–318.
Weertman, J., and J. R. Weertman (1975), High temperature creep of rock and mantle viscosity, *Annu. Rev. Earth Planet. Sci.*, *3*, 293.
Whittington, A., P. Richet, Y. Linard, and F. Holtz (2001), The viscosity of hydrous phonolites and trachytes, *Chem. Geol.*, *174*, 209–223.
Wilson, D. S., et al. (2006), Drilling to gabbro in intact ocean crust, *Science*, *312*(5776), 1016–1020, doi:10.1126/science.1126090.
Zhang, S., S. Cox, and M. Paterson (1994), The influence of room temperature deformation on porosity and permeability in calcite aggregates, *J. Geophys. Res.*, *99*, 761–775.
Zhu, W., and T. F. Wong (1997), The transition from brittle faulting to cataclastic flow: Permeability evolution, *J. Geophys. Res.*, *102*(B2), 3027–3041.
Zhu, W., M. K. Tivey, H. Gittings, and P. R. Craddock (2007), Permeability-porosity relationships in seafloor vent deposits: Dependence on pore evolution processes, *J. Geophys. Res.*, *112*, B05208, doi:10.1029/2006JB004716.
Zimmerman, M. E., and D. L. Kohlstedt (2004), Rheological properties of partially molten lherzolite, *J. Petrol.*, *45*(2), 275–298.
Zoback, M., and J. Byerlee (1975), The effect of microcrack dilatancy on the permeability of Westerly granite, *J. Geophys. Res.*, *80*, 752–755.

P. Azais, J.-M. Dautria, B. Gibert, D. Mainprice, and P. Pezard, Géosciences Montpellier UMR 5243, CNRS, Université Montpellier 2, Place Eugène Bataillon, F-34095 Montpellier CEDEX 05, France.
B. Evans, Department of Earth, Atmospheric, and Planetary Sciences, Massachusetts Institute of Technology, 77 Massachusetts Ave., Cambridge, MA 02139-4307, USA.
M. Violay, Istituto Nazionale di Geofisica e Vulcanologia, Via di Vigna Murata 605, I-00143 Roma, Italy. (marie.violay@ingv.it)